Exhibit A

(Part 3)

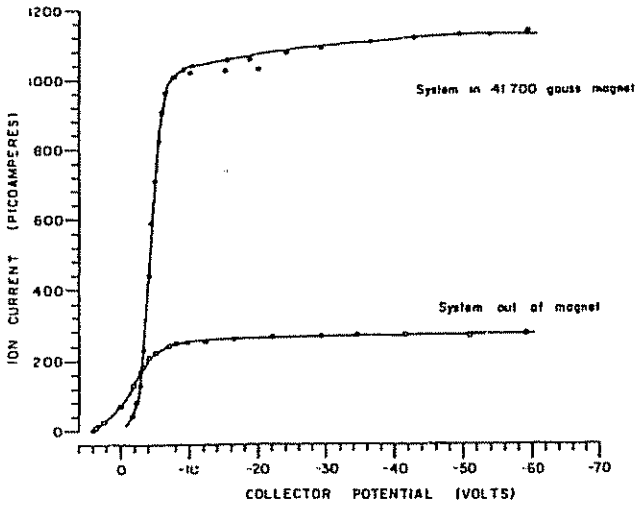

Fig. 2. Ion current transmitted to the analyzer cell as a function of the voltage applied to a collector plate of the cell.

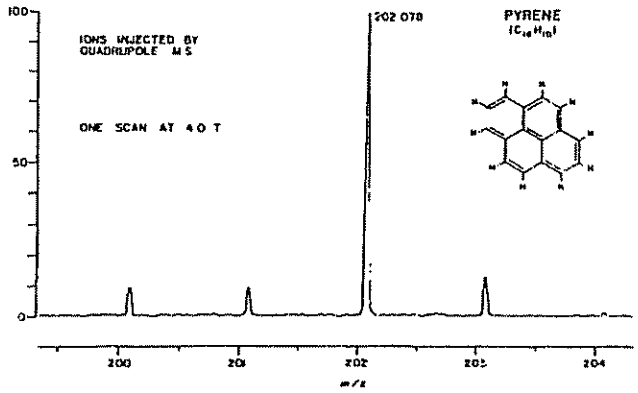

Fig. 3. FT–MS signals for pyrene ions injected by the quadrupole mass spectrometer into the analyzer cell.

beam so that it is not decelerated significantly by the magnetic mirror effect. In addition, the increases in ion current observed when the vacuum manifold is brought close to the magnet seems to be caused by collimation of the ion and electron beams in the ion source by the fringe fields of the magnet. Another important feature of Fig. 2 is the sharp drop in ion current at a retarding voltage of about −4 V. This indicates that the energy distribution of the ion beam is not broadened appreciably by the rf fields and the magnetic mirror effect.

Mass spectra showing the molecular ion region of pyrene are shown in Figs. 3 and 4. Figure 3 is an expanded portion of a single acquisition from *m/z* 185 to *m/z* 215 for ions injected from the source of the quadrupole mass spectrometer into the analyzer cell. Notice that the peak at *m/z* 203, the carbon-13 component of the pyrene molecular ion, has a relative abundance very close to the theoretical value of 17.8%. Even the peak at *m/z* 204, the molecular ion with two carbon-13 atoms, is very close to its theoretical relative abundance of 3.0%.

Figure 4 shows excellent signal-to-noise and mass resolution from a single 20 kHz narrow-band scan for the pyrene molecular ion at *m/z* 202. About 1 μg of pyrene placed on the direct insertion probe of the quadrupole mass spectrometer gave a very stable ion signal for several minutes.

Figure 5 shows QFT–MS signals for coronene. Very strong signals were obtained, even with one FT detection cycle, when the probe in the quadru-

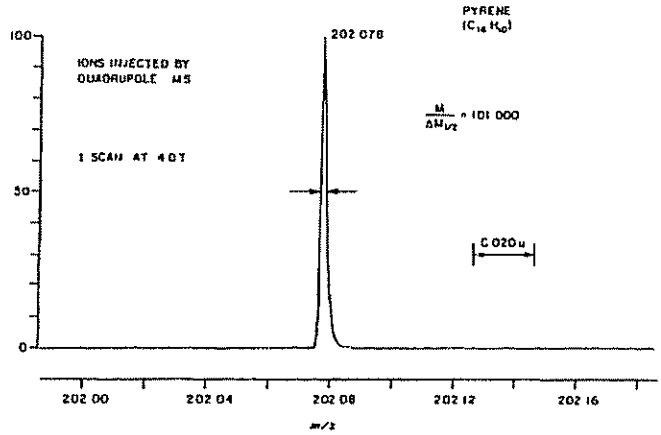

Fig. 4. High resolution QFT–MS signals for the molecular ion of pyrene

pole was at 140°C. Notice that the relative abundance of the carbon-13 peak height at m/z 301 is very close to its theoretical value of 26.6%. The elongated analyzer cell used in these studies seems to give better isotope ratios than a cubic cell used previously [18]. But with both cell designs, it is important to limit the number of ions in the analyzer cell to less than about 10^6–10^7. In our experience, ion space charge effects are the primary cause of incorrect isotope ratios.

Earlier, it was stated that the quadrupole rods could be used to select which ions are transmitted to the FT–MS analyzer cell. This is demonstrated in Fig. 6. The upper trace shows the intensity of the QFT–MS signal for m/z 202 from pyrene at various mass settings for the quadrupole rf unit. The lower trace shows similar data for m/z 300 from coronene. In these experiments, Q1 and Q2 were connected together and were operated in the rf-only mode. Both plots in Fig. 6 show that the quadrupole rods function as a bandpass filter for the ions. The transmission efficiency for m/z 300 maximizes at a mass setting of about 300, but decreases at lower and higher settings. Similar behavior is seen for m/z 202, but the maximum in the transmission curve is shifted to a mass setting of about 200.

Adding a differential d.c. voltage to the quadrupole rods narrows the bandpass and decreases the transmission efficiency, just as is expected for conventional quadrupole mass filters. When these experiments were first contemplated, it was feared that the intense magnetic field needed for FT–MS would interfere with the operation of the quadrupole mass filters.

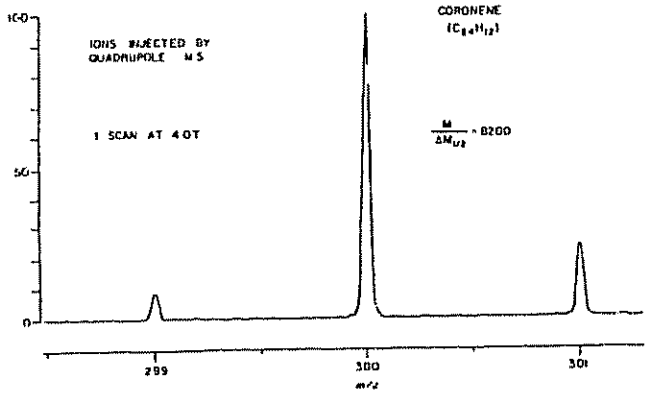

Fig. 5. QFT–MS signals for the molecular ion region of coronene

Fortunately, this turns out not to be the case. The operating parameters for the quadrupole ion source are typical and it seems that the fringe fields of the cryomagnet have little effect on the ions. Thus, a desirable situation has been realized in that the operating parameters for the tandem instrument are very similar to those of the separate instruments. The guiding quadrupole not only passes ions efficiently from Q1 to the FT–MS analyzer, but it also separates the two analyzers sufficiently for them to be adjusted and optimized independently.

Figure 1 shows that the QFT–MS instrument is conceptually similar to a triple quadrupole mass spectrometer [21,22]. The main difference is that, in QFT–MS, mass analysis and ion detection are performed by a Fourier transform analyzer cell instead of a third quadrupole and an electron multiplier. Collision-induced dissociation of ions, a powerful means for obtaining structural information, is readily performed with a triple quadrupole mass spectrometer and similar experiments can also be done with the

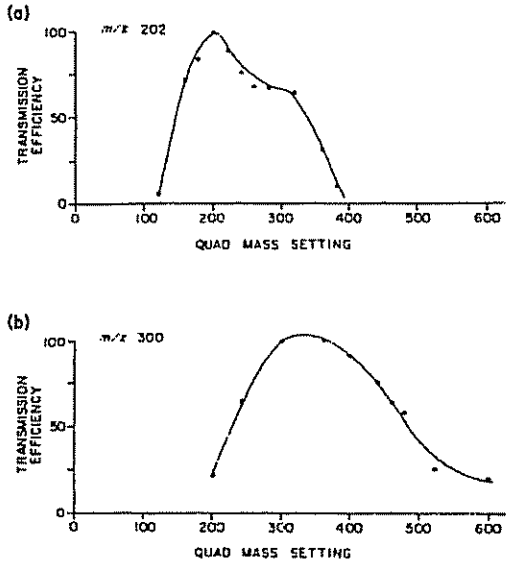

Fig 6. Transmission efficiency for ions injected by the quadrupole mass spectrometer into the FT–MS analyzer cell. Both Q1 and Q2 were operated in the rf-only mode (a) Injection of m/z 202; (b) injection of m/z 300.

QFT–MS instrument. Figure 7 is a mass spectrum of m/z 77 daughter ions formed by collision-induced dissociation of bromobenzene molecular ions. Nitrogen collision gas was pulsed into the manifold for 100 ms using an automobile fuel injector valve. The mass resolution shown in Fig. 7 is 140 000, over a thousand times better than can be achieved in daughter ion mass spectra recorded with triple quadrupole or sector MS/MS instruments [21–23].

In 1974, Smith and Futrell built a tandem mass spectrometer by coupling a Dempster mass analyzer with an ion cyclotron resonance (ICR) cell [24]. Subsequently, a similar instrument was constructed by Kemper and Bowers [25,26]. Both of these had high pressure ion sources and the ions were mass analyzed by magnetic deflection prior to being injected into the ICR analyzer cell. Fourier transform detection has not been performed with these instruments but, in principle, it is possible. Comparing the QFT–MS and tandem Dempster–ICR instruments, it appears that the QFT–MS concept will be more useful for analytical applications because it uses a high-field cryomagnet instead of a conventional electromagnet with pole caps. This not only provides higher mass resolution and ion trapping efficiency, but also allows greater access around the ion source of the quadrupole for coupling various interfaces.

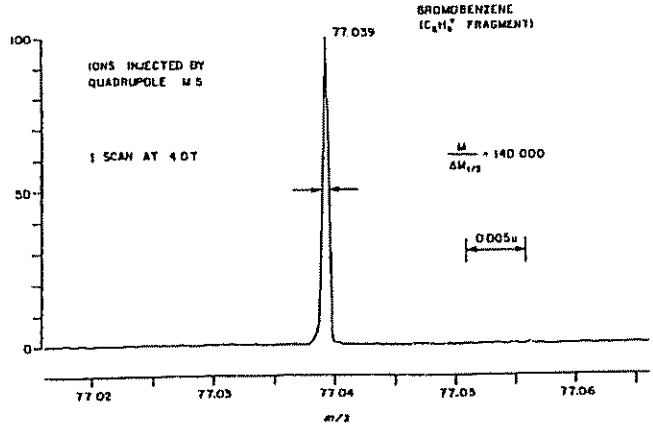

Fig. 7. Demonstration of MS/MS capabilities of the QFT–MS instrument. Daughter ions m/z 77 were produced by collision-induced dissociation of bromobenzene molecular ions by a pulse of N_2 collision gas.

An important use of the quadrupole rods in QFT–MS is to control the number of ions which are delivered to the FT–MS analyzer cell. In particular, ions such as the abundant glycerol peaks in FAB and the solvent cluster ions in LC would greatly overload the analyzer cell and causes space charge distortion of the FT signals. By pre-selecting which ions are passed to the analyzer cell, space charge effects can be minimized and the full dynamic range of the image current detector can be used for the ions of interest. Also, differential pumping in QFT–MS provides a low pressure in the FT–MS analyzer cell so that weak ion currents can be integrated for several seconds until a sufficient number of ions are accumulated for performing structure elucidation experiments utilizing laser photodissociation and collision-induced dissociation.

CONCLUSIONS

Preliminary results with QFT–MS are encouraging. The feasibility of injecting and detecting ions at high resolution has been demonstrated and it is clear that the quadrupole is capable of passing large ion currents to the FT–MS analyzer cell.

All our experiments with the prototype instrument have been conducted with a needle valve for adding liquid samples and a direct insertion probe for solids. The prototype instrument does not have a sufficient pumping capacity to handle a FAB gun or LC inlet, but appropriate modifications to the manifold will be made during the coming months so that these experiments can be attempted.

ACKNOWLEDGEMENTS

The equipment for these experiments was provided by the Finnigan Corporation. We are grateful to R.E. Finnigan, M.S. Story and J.W. Amy for technical assistance and support. Prof. D.F. Hunt, University of Virginia, has played a central role in defining the configuration and potential applications of QFT–MS.

REFERENCES

1 M.B. Comisarow and A.G. Marshall, Chem. Phys. Lett., 25 (1974) 282.
2 C.L. Wilkins, Anal. Chem., 50 (1978) 493A.
3 R.T. McIver, Jr., Am. Lab., 12 (11) (1980) 18.
4 C.L. Wilkins and M.L. Gross, Anal. Chem., 53 (1981) 1661A.
5 M.B. Comisarow, Int. J. Mass Spectrom. Ion Phys., 26 (1978) 369.
6 R.T. McIver, Jr., R.L. Hunter, E.B. Ledford, Jr., M.J. Locke and R.J. Francl, Int. J. Mass Spectrom. Ion Phys., 39 (1981) 65.

7 R.T. McIver, Jr. and W.D. Bowers, in F.W. McLafferty (Ed.), Tandem Mass Spectrometry, Wiley, New York, 1983.
8 R.B. Cody and B.S. Freiser, Int. J. Mass Spectrom. Ion Phys., 41 (1982) 199.
9 R.L. White and C.L. Wilkins, Anal. Chem., 54 (1982) 2211.
10 M.P. Irion, W.D. Bowers, R.L. Hunter, S. Delbert, F.S. Rowland and R.T. McIver, Jr., 31st Annu. Conf. Mass Spectrom. Allied Top., Boston, MA, 1983, Paper WOD 1.
11 R.B. Cody, R.C. Burnier, C.J. Cassady and B.S. Freiser, Anal. Chem. 54 (1982) 2225.
12 M.P. Irion, W.D. Bowers, R.L. Hunter, F.S. Rowland and R.T. McIver, Jr., Chem. Phys. Lett., 93 (1982) 375.
13 T.J. Carlin and B.S. Freiser, Anal. Chem., 55 (1983) 955.
14 T.J. Francl, M.G. Sherman, R.L. Hunter, M.L. Locke, W.D. Bowers and R.T. McIver, Jr., Int. J. Mass Spectrom. Ion Processes, 54 (1983) 189.
15 E.B. Ledford, S. Ghaderi, R.L. White, R.B. Spencer, P.S. Kulami, C.L. Wilkins and M.L. Gross, Anal. Chem., 52 (1980) 463.
16 R.L. White, E.C. Onyiriuka and C.L. Wilkins, Anal. Chem., 55 (1983) 339.
17 R.T. McIver, Jr., R.L. Hunter, M.S. Story, J. Syka and M. Labunsky, paper presented at 31st Annu. Conf. Mass Spectrom. Allied Top., Boston, MA, 1983.
18 R.L. Hunter, M.G. Sherman, R.T. McIver, Jr., Int. J. Mass Spectrom. Ion Phys., 50 (1983) 259.
19 F.F. Chen, Introduction to Plasma Physics, Plenum Press, New York, 1974, pp. 27–29.
20 R.T. McIver, Jr., unpublished work, 1982.
21 R.A. Yost and C.G. Enke, Anal. Chem., 51 (1979) 1251A.
22 F.W. McLafferty (Ed.), Tandem Mass Spectrometry, Wiley, New York, 1983.
23 G.L. Glish, S.A. McLuckey, T.Y. Ridley and R.G. Cooks, Int. J. Mass Spectrom. Ion Phys., 47 (1982) 157.
24 D.L. Smith and J.H. Futrell, Int. J. Mass Spectrom. Ion Phys., 14 (1974) 171.
25 P.R. Kemper and M.T. Bowers, in H. Hartmann and K.-P. Wanczek (Eds.), Ion Cyclotron Resonance Spectrometry, Lecture Notes in Chemistry, Vol. 31, Springer, Berlin, 1982, p. 308.
26 P.R. Kemper and M.T. Bowers, Int. J. Mass Spectrom. Ion Phys., 52 (1983) 1.

ACKNOWLEDGEMENTS

The authors acknowledge with thanks the financial support of this work by the Swedish Natural Science Research Council and the National Swedish Board for Technical Development. The authors are also grateful to Mats Lundell for typing the manuscript and drawing some of the figures

REFERENCES

1 I. Szabo, Int J Mass Spectrom Ion Processes, 73 (1986) 197
2 M H Friedman, A.L Yergey and J F Campana, J Phys E, 15 (1982) 53
3 P H Dawson (Ed.), Quadrupole Mass Spectrometry and Its Applications, Elsevier, Amsterdam, 1976
4 P H Dawson and N R Whetten, in D Price (Ed.), Dynamic Mass Spectrometry, Vol. 2, Heyden, London, 1971
5 C Hägg and I Szabo Int J Mass Spectrom Ion Processes, 73 (1986) 237
6 I. Szabo, Int J Mass Spectrom. Ion Processes, submitted for publication
7 R.A Howard, Dynamic Probalistic Systems, Vols I and II, Wiley, New York, 1971
8 C. Hägg and I. Szabo, Int J Mass Spectrom Ion Processes, 73 (1986) 295

International Journal of Mass Spectrometry and Ion Processes, 73 (1986) 295–312 295
Elsevier Science Publishers B V., Amsterdam – Printed in The Netherlands

NEW ION-OPTICAL DEVICES UTILIZING OSCILLATORY ELECTRIC FIELDS. IV. COMPUTER SIMULATIONS OF THE TRANSPORT OF AN ION BEAM THROUGH AN IDEAL QUADRUPOLE, HEXAPOLE, AND OCTOPOLE OPERATING IN THE RF-ONLY MODE

CONNY HÄGG and IMRE SZABO *

Division of Physical Chemistry 2, Chemical Center, The University of Lund, P O. Box 124, S-221 00 Lund (Sweden)

(Received 1 July 1986)

ABSTRACT

The passage of several ensembles of ions through an ideal electric quadrupole, hexapole, and octopole operating in the rf-only mode has been simulated on a computer by solving numerically the appropriate equations of motion *for* each ion in the ensemble The molecular weight was chosen to be 50, 145, and 1000 u in the different ensembles The remaining assumptions are as follows (1) The initial distribution of transverse velocities of ions is Maxwellian and corresponds to 500 K. (2) The initial positions of ions having different initial velocities are randomly and uniformly distributed at the entrance hole. (3) The quadrupole, hexapole, and octopole fields are generated by pure a.c voltages (rf-only mode) whose amplitudes are either identical or close to the value set by the upper limit of stability for the device in question

The following quantities were calculated *for* the ensembles of ions: (1) transverse displacements, (2) transverse kinetic energies, and (3) cross-sections of the ion beam along the beam axis. The results show that the electric hexapole and octopole are more suitable for transporting and confining ion beams than is the quadrupole.

1 INTRODUCTION

The electric quadrupole mass filter operating in the rf-only mode has, during recent years, attracted growing interest in sequential mass spectrometry [1–8]. It is used not only in triple quadrupole mass spectrometers where

* To whom correspondence should be addressed.

0168-1176/86/$03 50

the central quadrupole is operating in the rf-only mode [1,2,4], but also in multistage hybrid-type mass spectrometers [5–8]. In these applications, the rf-only mode quadrupole is used to confine beams of ions having low translational energies, generally below 100 eV. The ions passing through the rf-only mode quadrupole may dissociate upon collisions with a target gas [1,2,4] (collisionally activated dissociation, CAD) or by absorption of photons [9]. Therefore, it is desirable that the device is capable of simultaneously confining ions whose molecular weights extend over a large mass range, i.e. it can simultaneously confine both parent ions and fragment ions as well as ions formed by ion/molecule reactions. The confinement of ions in a quadrupole operating in the rf-only mode has recently been investigated by Dawson and Fulford [4].

The application of an octopole operating in the rf-only mode for guiding ion beams was pioneered by Teloy and Gerlich [10] over a decade ago. The octopole was used for studying integral cross-sections of ion/molecule reactions. At present, the same device is used, e.g. in the guided ion beam tandem mass spectrometer [11] and in a flow drift tube apparatus [12]. The electrode geometry of the quadrupole analyser can easily be generalized in order to obtain a whole family of multipole devices consisting of $2p$ electrodes ($p = 2, 3, 4, \ldots$) [13,14]. Here, p is the number of pairs of poles.

In our laboratory, ion motion in the two-dimensional oscillatory electric hexapole [15] and octopole [16] field has been simulated by solving numerically the appropriate equations of motion [13,14]. These calculations show unambiguously that multipoles consisting of $2p > 4$ electrodes and operating in the a.c. + d.c. mode (like the quadrupole mass analyser) are not suited for mass analysis. However, the results discussed in the present paper prove that the hexapole and the octopole (and probably also multipoles of even higher order) are much more suited for guiding and confining beams of ions than is the quadrupole ($2p = 4$). The explanation is that the restoring force acting on an ion in a multipole field of order p is proportional to r^{p-1} [13] where r is the minimum distance measured from the instrument axis to the ion.

This paper summarizes the results of our computer simulations regarding the transport of three different ensembles of ions through the ideal quadrupole, hexapole, and octopole operating in the rf-only mode. The main result is that, instead of a quadrupole, which is exclusively used at present in many applications [1–9], it would be more advantageous to use a hexapole or even an octopole for transporting and confining beams of ions. In this paper, the multipoles of different order are treated individually and their coupling with other ion optical devices, e.g. matching a quadrupole operating in the mass filter mode with a hexapole or octopole, will be the subject of a future project in our laboratory.

2 THE CALCULATIONS

2.1 The equations of motion

The motion of an ion in a two-dimensional multipole field of order p in the Cartesian system of coordinates is given by the following set of equations [13], provided that the plane of symmetry for one of the positively biased electrodes coincides with the positive x axis.

$$\frac{d^2X}{dT^2} + \left[a_p - 2q_p \cos p(T - T_0)\right] \left[\binom{p-1}{0} X^{p-1}Y^0 - \binom{p-1}{2} X^{p-3}Y^2 + \binom{p-1}{4} X^{p-5}Y^4 - \ldots\right] = 0 \quad (1)$$

$$\frac{d^2Y}{dT^2} - \left[a_p - 2q_p \cos p(T - T_0)\right] \left[\binom{p-1}{1} X^{p-2}Y^1 - \binom{p-1}{3} X^{p-4}Y^3 + \binom{p-1}{5} X^{p-6}Y^5 - \ldots\right] = 0 \quad (2)$$

$$X = \frac{x}{r_0}, \; Y = \frac{y}{r_0}, \; T = \frac{\omega t}{p}, \; T_0 = \frac{\omega t_0}{p} \quad (3)$$

and

$$a_p = \frac{p^2 eU}{2m\omega^2 r_0^2} \qquad q_p = \frac{p^2 eV}{4m\omega^2 r_0^2} \quad (4)$$

Here, r_0 is the radius of the instrument aperture (one half of the shortest distance between opposite rods). $\omega = 2\pi f$ is the angular frequency and f is the frequency of the applied field. T_0 is the time when the ion, having the molecular weight m, first experiences the field, i.e. the field entrance phase. V is the zero-to-peak rf voltage which is superimposed on a static (d.c.) voltage U. Detailed studies of the ion motion in the quadrupole [17] ($p = 2$), hexapole [15] ($p = 3$), and octopole [16] ($p = 4$) field have previously been carried out by solving numerically the appropriate equations of motion.

2.2 Initial conditions

Three different ensembles, each consisting of 1000 identical, singly charged and non-interacting ions, were generated by sampling initial transverse velocities from the two-dimensional Maxwellian distribution of speeds at 500 K. The molecular weight was assumed to be 50, 145, and 1000 atomic mass units, u, respectively. Figure 1 shows the sampled distributions for the

TABLE 1

Multipole parameters used in the calculations

Field radius	$r_0 = 2.52 \times 10^{-3}$ m
A.C. frequency	$f = 1.8 \times 10^{6}$ s^{-1}
D.C. voltage	$U = 0$ V ($\alpha = 0$)
Electronic charge	$e = 1.602192 \times 10^{-19}$ As
Atomic mass unit	$u = 1.660565 \times 10^{-27}$ kg

Condition	Entrance hole	q_3	q_5	q_4	q_4/ρ^4	V/m (volt/mass unit)
1	$0.1r_0$	0.1289	0.4350	1.0311	0.0161111	0.54254
2	$0.1r_0$	0.5000	1.6875	4.0000	0.0625000	2.1047
3	$0.1r_0$	0.8889	3.0000	7.1111	0.1111111	3.7417
4	$0.1r_0$		5.0000	50.000	0.185185	6.2361
5	$0.1r_0$				0.781250	26.399

[a] Taken from ref. 27.

having their speeds and velocities in the range c to $c + \Delta c$ and v to $v + \Delta v$, respectively. The increments Δc and Δv are equal to 50 m s^{-1} in Fig. 1(a) and 20 m s^{-1} in Fig. 1(b). The initial positions of ions in an ensemble will be randomly and uniformly distributed on the circular entrance hole whose origin coincides with the instrument axis and radii are assumed to be $0.1r_0$, $0.2r_0$, or $0.3r_0$ as specified in the text that follows.

The performance of the quadrupole, hexapole, and octopole will be compared for five different sets of the parameters q_n [Eq. (4)] compiled in Table 1 and called conditions 1–5. Equivalent operating conditions (such as conditions 1, 2 or 3) are obtained when the ratio

$$\frac{q_n}{\rho^p} = \frac{eV}{4m\omega^2 r_0^2} \qquad \text{for } p = 2, 3, 4, \ldots \tag{5}$$

is a constant number, i.e. the same set of system parameters V/m, ω, and r_0 applies. The ratio q_n/ρ^p increases gradually in Table 1 when going from condition 1 to condition 5. When condition 2 applies, the quadrupole operates close to its stability limit [19], which corresponds to $q_{2\max} = 0.908046$. The upper limit for stability slightly exceeds $q_3 = 5.0$ for the hexapole [15] (condition 4) and $q_4 = 50.0$ for the octopole [16] (condition 5). Thus, conditions 3–5 allow us to compare the performance of the quadrupole, hexapole, and octopole operating close to the upper limit of their stability.

The time of integration for each ion in the ensembles was taken to be twenty rf cycles.

Fig. 1. Sampled distributions of initial speeds ($c = r_0^2 + r_0^2$) and velocity components (v and v, broken line) corresponding to 500 K. The molecular weight is (a) 145 u and (b) 1000 u. Numbers 145 and 1000 u together with the corresponding calculated Maxwellian distributions [18] $f(c)$ and $f(r)$. Here, $c = (r_0^2 + v_0^2)^{1/2}$, $r = r_0$ or r_0, N is the total number of ions in the ensemble, and n is the number of ions

3. RESULTS

3.1 Displacement of ions perpendicularly to the beam axis

The displacements of ions perpendicularly to the beam axis have been calculated for three different sets of equivalent operating conditions determined by conditions 1–3 in Table 1. Approximate values of the largest ion displacements found are compiled in Table 2. These exhibit only minor variations for the same molecular weight when condition 1 or condition 2 applies. However, in case of condition 3, the largest ion displacement in the quadrupole equals the field radius r_0 and a small percentage of the ions is lost upon collision with the electrode surfaces. In contrast, in the hexapole and octopole operating according to condition 3, the maximum ion displacement is considerably smaller and none of the ions is lost. The explanation is that the quadrupole operates close to its stability limit while the hexapole and octopole are far from the corresponding stability limits.

3.2 Ion beam cross-sections

We have also determined the transverse cross-section of the beam of ions having the molecular weight 145 u at several positions along the beam axis (i.e. at different times, pT). These cross-sections are visualized by setting a dot at the instantaneous position of the ion in the (x, y) plane which is perpendicular to the beam axis. Some of the results of our computations corresponding to condition 3 are shown in Figs. 2–4. The ion beam cross-sections shown in this paper were obtained by superimposing four of those cross-sections which correspond to 1000 ions for each of the field entrance phases $pT_0 = 0, \pi/2, \pi$, and $3\pi/2$, respectively. This procedure has been adopted in order to approximate a continuous ion beam. If the frequency of the rf field is chosen to be 1.8 MHz as indicated in Table 1, then the total number of ions in the beam corresponds to an ion current of about 10^{-9} A.

Figure 2 shows the cross-section of the ion beam for the fourth period of the rf cycle, as indicated by the given numerical values of the argument 27. The largest cross-sections are obtained during this period of the time. About four periods later, the ion beam becomes focused to its smallest cross-section as shown in Fig. 3. These cross-sections and the area of the entrance hole, $(0.1r_0)^2\pi$, are about of the same size. When ions are travelling down the beam axis, the cross-section of the beam will oscillate between these two extremes. The period of this oscillation along the beam axis is about 16π, provided that $q_z = 0.8889$ in accordance with condition 3. The computed cross-sections in Figs. 2 and 3 are in agreement with earlier experimental

TABLE 2

Approximate maximum ion displacement in a quadrupole, hexapole, and octopole operating at equivalent system parameters corresponding to conditions 1–3 in Table 1

Molecular weight	Condition 1 ($q_z/p^2 = 0.0161111$)				Condition 2 ($q_z/p^2 = 0.0625000$)				Condition 3 ($q_z/p^2 = 0.111111$)			
	U (V)	$p = 2$	$p = 3$	$p = 4$	U (V)	$p = 2$	$p = 3$	$p = 4$	U (V)	$p = 2$	$p = 3$	$p = 4$
50	27.1	$0.80r_0$	$0.75r_0$	$0.75r_0$	105.2	$0.35r_0$	$0.45r_0$	$0.50r_0$	187.1	r_0	$0.30r_0$	$0.40r_0$
145	78.7	$0.60r_0$	$0.55r_0$	$0.60r_0$	305.2	$0.25r_0$	$0.30r_0$	$0.40r_0$	542.5	r_0	$0.25r_0$	$0.35r_0$
1000	542.5	$0.25r_0$	$0.35r_0$	$0.45r_0$	2104.7	$0.25r_0$	$0.21r_0$	$0.30r_0$	3741.7	r_0	$0.15r_0$	$0.25r_0$

Fig. 2. Computed cross-sections of an ion beam at four different instants of the time (2T) during the fourth rf cycle in a quadrupole ($p = 2$) which operates in the *rf*-only mode according to condition 3 (Table 1). The molecular weight of the ion is 145 u.

[19] and theoretical [20] results. However, for q_z values corresponding to conditions 1 and 2, the largest ion beam cross-section becomes smaller, as seen from the data in Table 2.

The cross-sections of the same ion beam in the hexapole and octopole, operating in accordance with condition 3 in Table 1, are shown in Fig. 4(a) and (b), respectively. The main result is that the cross-section of the beam does not vary significantly and is almost circular along the beam axis. This contrasts with the cross-section of the same beam in the quadrupole which oscillates as shown in Figs. 2 and 3.

Our results in Figs. 5 and 6 show that the ion beam remains almost cylindrical in the hexapole and octopole, even if they are operating close to

Fig. 5. Computed cross-sections of an ion beam at four different instants of the time (2T) during the eighth rf cycle in a quadrupole. The operating conditions are the same as in Fig. 2.

the upper limits of their stability, i.e. in according with conditions 4 and 5, respectively, given in Table 1. As seen from Figs. 5 and 6, a few ions are displaced relatively far away from the beam axis. These ions are on their way to leave the interelectrode space and to be lost because they execute unstable oscillations. In conclusion, the hexapole and octopole operating in the rf-only mode are more suited than the quadrupole for confining and merging, e.g. an ion beam/laser beam, ion beam/molecule beam and ion beam/electron beam.

J J Transmission characteristics

The transmission of ions, i.e. the ratio between the number of outgoing and incoming ions, was calculated for various q_z values, entrance holes, and

Fig. 4. Computed ion beam cross-section in (a) an rf-only mode hexapole ($p = 3$) and (b) an rf-only mode octopole ($p = 4$) corresponding to condition 3 and molecular weight 145 u

initial phases (pT_0) for ion entrance. Figure 7 shows the computed transmission curves for the beams which are illustrated in Figs. 2, 3, 5, and 6. The conditions which apply are summarized in Table 1. As seen, the ion loss for the octopole is about 20% during the simulation time. Thus indicates that q_4 should be less than 50 in order to ensure a high transmission of ions in addition to good confinement. By comparing Figs. 4–6, we find that the

Fig. 5. Computed ion beam cross-section in an rf-only mode hexapole ($p = 3$) corresponding to condition 4 and molecular weight 145 u. The beam is shown at (a) $37 = 24\pi$ and (b) $37 = 40\pi$

Fig. 6. Computed ion beam cross-section in an rf-only mode octopole ($p = 4$) corresponding to condition 3 and molecular weight 145 u. The beam is shown at (a) $47 = 24\pi$ and (b) $47 = 40\pi$

beam cross-sections are almost insensitive to the choice of q_3 and q_4 and that they remain small if the ions enter the devices relatively close to the instrument axis. However, if the q_3 and q_4 values become relatively large, some ions will be lost due to the instability of their paths. This instability strongly depends on the entrance conditions (position, velocity, and field phase) of the ions as shown previously [15,16].

Table 3 shows the transmission of an ensemble of ions (molecular weight 145 u) which enters the multipole devices via an entrance hole whose radius is chosen to be $0.1r_0$, $0.2r_0$, and $0.3r_0$, respectively. The transmission of ions has been determined for 20 cycles of the rf field. As seen from Table 3, the passage of the ions through the multipole devices is strongly favoured if an octopole is used. The ions executing stable oscillations in the hexapole and octopole will be confined relatively close to the instrument axis so that the

TABLE 3

Transmission of ions (145 u) in a twenty rf cycles long quadrupole, hexapole, and octopole operating in the rf-only mode

Radius of entrance hole	Transmission (%) $q_3/p^2 = 0.111111$			
	$p = 2$	$p = 3$	$p = 4$	
$0.1r_0$	95	100	100	
$0.2r_0$	55	90	100	
$0.3r_0$	30	55	95	

beam radius does not exceed about $0.4r_0$ if the radius of the entrance hole is $0.2r_0$. If the radius of the entrance hole is $0.3r_0$, the beam radius remains less than about $0.5r_0$.

3.4 Kinetic energies of ion motion perpendicular to the beam axis

The transverse kinetic energies of the ions (molecular weight 145 u) travelling through the quadrupole, hexapole, and octopole operating in accordance with condition 3 in Table 1 were computed for the field entrance phase $\rho T_0 = 0$. Figure 8 shows the variation of the average energy per ion, $\langle E \rangle$, for the ensemble consisting of 1000 ions. The subscripts x and y stand for the transverse kinetic energy in the x and y directions, respectively.

Fig. 7. Computed transmission for ions (145 u) in (a) a quadrupole (condition 3), (b) a hexapole (condition 4), and (c) an octopole (condition 5). The initial phases (ρT_0) for ion entrance are given as parameters.

Fig. 7 (continued)

while E_T is the total transverse kinetic energy. In the quadrupole (Fig. 8(a)), very high transverse kinetic energies are observed compared with the hexapole (Fig. 8(b)) and octopole (Fig. 8(c)). The transverse kinetic energy for ions in the quadrupole depends explicitly on the field entrance phase, $2T_0$. For example, if the field entrance phase is $2T_0 = \pi/2$ or $3\pi/2$, the maximum transverse energies ($\langle E_x \rangle$ and $\langle E_y \rangle$) will be about 30 eV each, while the maximum total energy will be about 60 eV. For the field phase $2T_0 = \pi$, the curves showing the transverse kinetic energy in the x and y directions of Fig. 8(a) become interchanged. The transverse kinetic energy in the quadrupole is large because the device operates close to its stability limit. For low q_z values, the transverse kinetic energy of the ions in the beam will be considerably lower. Calculations in our laboratory (not reproduced in this paper) show that the transverse kinetic energy in an rf-only mode quadrupole varies between about 0.1 and 0.5 eV for $q_z < 0.75$, while the kinetic energy in the hexapole and octopole will be about 0.1 eV and almost independent of the numerical values of q_z, q_x, and the field entrance phase.

3.5 Initial conditions and the upper limit for stability

The size and shape of the (a_x, q_x) stability diagram for the hexapole ($p = 3$) [15] and octopole ($p = 4$) [16] depend on the initial position.

Fig. 8. Computed mean transverse kinetic energies $\langle E_\perp \rangle$, $(E_\perp)$ and $(E_\perp)$ (broken lines) for ions (condition 3 and molecular weight 145 u) in (a) a quadrupole, (b) a hexapole, and (c) an octopole. The ions enter the multipoles at zero field phase and with a mean transverse kinetic energy $(E_\perp) = 0.023$ eV and $(E_\perp) = 0.020$ eV.

velocity, and phase for ion entrance. The results [15,16] presented so far refer to the initial phase $\rho T_0 = 0$. Figure 9 in this paper shows the variation of the upper limit for stability (i.e. the maximum value of q_z for stable ion trajectories at $a_z = 0$) when the field entrance phase and initial position is changed. Computations were made for the hexapole [Fig. 9(a) and (b)] and for the octopole [Fig. 9(c) and (d)] at a series of fixed values of the initial positions (R, θ where $R^2 = X^2 + Y^2$), assuming the initial velocities $v_z = v_\perp$ = 0. Here, the distance from the instrument axis is $R = r/r_0 = 0.1$ for Fig. 9(a) and (c) and 0.2 for Fig. 9(b) and (d). The polar angle is $\theta = k\pi/(4\rho)$

Fig. 9. The dependence of the maximum values of q_z and q_x on the r.f. entrance phase angle (ρT_0) and initial position (R, θ). For the hexapole when (a) $R = 0.1$ and (b) $R = 0.2$. For the octopole when (c) $R = 0.1$ and (d) $R = 0.2$.

with $k = 0, 1, 2, 3$ or 4. If $k = 0$, it means that the initial position for the ion coincides with the plane of symmetry for a positively biased electrode, while for $k = 4$, the initial position coincides with the plane of symmetry for a negatively biased electrode. The curves in Fig. 9 refer to different numerical values of the phase $\rho T_0 = 0$, $\pi/2$, π, or $3\pi/2$ as indicated. The methods of computation employed have been thoroughly discussed in the previous papers [13,15,16] in this series.

The maximum values of q_3 and q_4, respectively displayed in Fig. 9 for different numerical values of the field entrance phase pT_0, exhibit a periodic behaviour as a function of θ. When the initial phase $pT_0 = 0$, the maximum values of q_3 and q_4 increase rapidly with increasing θ. The physical explanation for this behaviour is that a positively charged ion, starting its motion with $v_z = 0$ at $T = 0$ and $\theta = 0$, will first be accelerated towards the electrode. Thus radial acceleration decreases gradually with increasing θ, becomes zero at $\theta = \pi/(2p)$ and will be directed towards the beam axis in front of the negatively biased electrode. It reaches a maximum value at $\theta = \pi/p$, i.e. in the plane of symmetry for the negatively biased electrode. The opposite behaviour is observed when the initial phase is $pT_0 = \pi$ instead of zero. On the other hand, the variation of q_3 and q_4 with θ will be less pronounced for $pT_0 = \pi/2$ and $pT_0 = 3\pi/2$, respectively, because these cases represent intermediate situations compared with the two extremes ($pT_0 = 0$ or π) referred to above.

When operating in the rf-only mode, the molecular weight of the lightest ion (associated with stable trajectories) which can pass through a hexapole or an octopole, is determined by the maximum value of q_3 and q_4, respectively [cf. Eq. (4)]. Consequently, we obtain the following results if we have equivalent entrance and operating conditions. The mass range for the ions which can be confined simultaneously will be larger for the octopole [Fig. 9(c) and (d)] than for the hexapole [Fig. 9(a) and (b)]. The corresponding mass range is much smaller for the quadrupole because the maximum value of q_z is only 0.908 [19]. The octopole and the hexapole are more suited than the quadrupole for several applications in gas-phase ion chemistry and ion physics. These applications will be mentioned below.

4. CONCLUSIONS

The following main features were found for a quadrupole, hexapole, and octopole operating in the rf-only mode and used for confining and transporting a beam of ions.

(1) In the case of equivalent operating conditions, all three devices exhibit about the same performance as long as the ratio $q_z/p^2 < 0.1125$, which corresponds to the upper limit of stability ($q_z < 0.9$) for the quadrupole.

(2) The quadrupole, hexapole, and octopole become unstable one after the other when the ratio q_z/p^2 increases (cf. conditions 1–5 in Table 1). The ion beam in the hexapole and octopole can be confined relatively close to the instrument axis so that the beam has a nearly circular cross-section, even if q_3 and q_4, respectively, are close to the upper limit of stability (cf. conditions 4 and 5 in Table 1 and Figs. 4–6). However, the ions must enter

relatively close ($r < 0.3r_0$) to the axis of the instrument in order to ensure high transmission.

(3) In a hexapole and in an octopole, even those ions which exhibit relatively large differences in mass can simultaneously be confined close to the instrument axis. In contrast to the quadrupole (Figs. 2 and 3), the ion density along this axis can be relatively high because the beam does not execute any appreciable radial oscillations.

The above features make the hexapole, and especially the octopole, particularly suitable for the following applications.

(1) In tandem mass spectrometry [1–8] (MS/MS), a quadrupole is often used as a collision cell for investigating the dissociation of mass-selected ions induced by collisions at low translational energies (E_{lab} < about 100 eV). During the dissociation, there is a sudden decrease in ion mass and a corresponding sudden increase of q_z for the product ion. The ions for which $q_z > 0.908$ will be lost because their trajectories will become unstable. On the other hand, if the dissociation takes place in a hexapole or an octopole, it is possible to retain even those ions for which the values of q_3 and q_4, respectively, are relatively high.

(2) In gas-phase ion chemistry, ion spectroscopy, and ion physics, it is more advantageous to use a hexapole and an octopole instead of quadrupole, e.g. for studying the following atomic and molecular processes. (i) Interactions between mass-selected ions and photons (i.e. laser and synchrotron radiation); (ii) ion/molecule reactions in merged beams; (iii) chemiluminescent ion/molecule exchange reactions [21] and charge-exchange reactions [22].

(3) In Fourier transform mass spectrometry, it is possible to use a hexapole or an octopole for guiding a beam of mass-selected ions into the analyser cell placed in the bore of a solenoid-type superconducting magnet [23]. McIver et al. [24] have suggested the use of an rf-only mode quadrupole for this purpose.

According to recent studies in our laboratory [25,26], continuous or pulsed beams of ions whose mass and internal energy are known can conveniently be produced via charge-exchange reactions at low kinetic energies in a tandem mass spectrometer of perpendicular type. Thus, in the future, the mass-selected ions used in the above applications can be replaced by ions whose internal energy states are also known.

ACKNOWLEDGEMENTS

This research has been supported by grants from the Swedish Natural Science Research Council and the National Swedish Board for Technical Development. The authors thank also Mr. Mats Lundell for valuable assistance.

REFERENCES

1 P.H. Dawson and D.J. Douglas, in F.W. McLafferty (Ed.), Tandem Mass Spectrometry, Wiley, New York, 1983, p. 125.
2 R.A. Yost and C.G. Enke, in F.W. McLafferty (Ed.), Tandem Mass Spectrometry, Wiley, New York, 1983, p. 175
3 M.W. Siegel in F.W. McLafferty (Ed.), Tandem Mass Spectrometry, Wiley, New York, 1983, p. 371.
4 P.H. Dawson and J.E. Fulford, Int. J. Mass Spectrom Ion Phys., 42 (1982) 195
5 G.L. Glish, S.A. McLuckey, T.Y. Ridley and R.G. Cooks, Int. J. Mass Spectrom Ion Phys., 41 (1982) 157.
6 R.A. Yost and D.D. Fetterolf, Mass Spectrom. Rev., 2 (1983) 1
7 J.H. Beynon, F.M. Harris, B.N. Green and R.H. Bateman, Org. Mass Spectrom., 17 (1982) 55.
8 R.G. Cooks Anal. Chem., 57 (1985) 823A.
9 D.C. McGilvery and J.D. Morrison, Int. J. Mass Spectrom. Ion Phys., 28 (1978) 81.
10 E. Teloy and D. Gerlich, Chem. Phys., 4 (1974) 417.
11 K.M. Ervin and P.B. Armentrout, J. Chem. Phys., 83 (1985) 166.
12 H. Villinger, J.H. Futrell, A. Saxer, R. Richter and W. Lindinger, J. Chem. Phys., 80 (1984) 2543.
13 I. Szabo, Int. J. Mass Spectrom. Ion Processes, 73 (1986) 197.
14 M.H. Friedman, A.L. Yergey and J.E. Campana, J. Phys. E, 15 (1982) 53.
15 C. Hagg and I. Szabo, Int. J. Mass Spectrom. Ion Processes, 73 (1986) 237
16 C. Hagg and I. Szabo, Int. J. Mass Spectrom Ion Processes, 73 (1986) 277.
17 P.H. Dawson (Ed.), Quadrupole Mass Spectrometry and its Applications, Elsevier, Amsterdam, 1976
18 W.J. Moore, Physical Chemistry, Longmans, London, 1976, p. 139
19 I.L.E. Weaver and G.E. Mabbett, in D. Price and J.F.J. Todd (Eds.), Dynamical Mass Spectrometry, Vol. 5, Heyden, London, 1978, p. 41
20 J.F.J. Todd, R.M. Waldren, D.A. Freer and R.B. Turner, Int. J. Mass Spectrom Ion Phys., 35 (1980) 107
21 Ch. Ottinger, in M.T. Bowers (Ed.), Gas Phase Ion Chemistry, Vol. 2, Academic Press, New York, 1984, p. 249.
22 J.J. Leventhal, M.T. Bowers (Ed.), Gas Phase Ion Chemistry, Vol. 3, Academic Press, New York, 1984, p. 309
23 I. Szabo, Int. J. Mass Spectrom Ion Processes, submitted for publication
24 R.T. McIver, R.L. Hunter and W.D. Bowers, Int. J. Mass Spectrom. Ion Processes, 64 (1985) 67.
25 I. Szabo, in J. Berkowitz and K.-O. Groeneveld (Eds.), Molecular Ions Geometric and Electronic Structures, Plenum Press, New York, 1983, p. 517
26 I. Szabo, Nucl. Instrum. Methods Phys. Res. Sect. A, 239 (1985) 139
27 E.R. Cohen and B.N. Taylor, J. Phys. Chem. Ref. Data, 2 (1973) 663.

International Journal of Mass Spectrometry and Ion Processes, 73 (1986) 313–322 313
Elsevier Science Publishers B.V., Amsterdam – Printed in The Netherlands

COLLIMATOR EFFICIENCY IN LASER VAPORIZATION SYSTEMS USING MASS SPECTROMETRIC DETECTION

H. OHASHI
Department of Nuclear Engineering, Hokkaido University, Sapporo (Japan)

S.K. YAGNIK and D.R. OLANDER
Materials and Molecular Research Division, Lawrence Berkeley Laboratory and the Department of Nuclear Engineering, University of California, Berkeley, CA 94720 (U.S.A.)

(First received 16 June 1986; in final form 4 August 1986)

ABSTRACT

High-temperature vaporization characteristics of refractory solids are often investigated using laser pulse heating and mass spectrometric detection. The geometry of the vaporizing surface, collimator, and the detector is an important consideration in interpreting such experimental results. The mass spectrometer signal depends on the radial dependence both in the laser beam power density and of the relative effectiveness of off-center radial positions on the surface in contributing to the total signal. The function characterizing the latter effect is called the collimator function. Its measurement and application to a typical laser evaporation experimental system has been described.

INTRODUCTION

Experimental systems designed to characterize vaporization of refractory materials at very high temperatures often employ laser pulse heating of the solid and mass-spectrometric detection of the vaporized species [1–3]. To make this technique quantitative, extensive calibrations of the mass spectrometer and of the laser are necessary.

The geometry of the vaporizing surface and the detector is shown in Fig. 1. A collimator is placed between these two in order to define the spot on the surface which is viewed by the mass spectrometer and to prevent the latter from being contaminated by the blow-off from the surface. The apparatus is operated under high vacuum, so that free molecular flow prevails. Because of the surface–collimator–detector geometry, vaporization from off-axis radial locations on the surface is less likely to produce a signal in the mass spectrometer than positions close to the center line. In fact, beyond the radial position, denoted by R_m in Fig. 1, emitted particles cannot enter the detector at all. To account for this geometric phenomenon,

0168-1176/86/$03.50

TA 86

T005854

Capillary Zone Electrophoresis–Mass Spectrometry Using an Electrospray Ionization Interface

Richard D. Smith,* José A. Olivares,[1] Nhung T. Nguyen, and Harold R. Udseth

Chemical Methods and Separations Group, Chemical Sciences Department, Pacific Northwest Laboratory, Richland, Washington 99352

Instrumentation developed for capillary zone electrophoresis–mass spectrometry (CZE–MS) is described. The interface is based upon direct electrospray ionization from the end of the CZE capillary. The electrospray ionization source functions at atmospheric pressure and provides excellent sensitivity for wide ranges of compounds, with detection limits generally in the femtomole range (although significant improvements appear feasible). The instrumentation allows the high separation efficiencies feasible with CZE to be exploited and offers potential advantages compared with LC–MS methods, particularly when only small samples are available or high-resolution separations are necessary. The performance of the electrospray interface and the techniques and operating conditions for CZE–MS separations are described. CZE–MS separations and mass spectra are shown for mixtures that include polypeptides and quaternary ammonium salts. Separation efficiencies and detection limits vary widely from compound to compound and are shown to be sensitive to buffer selection. Separation efficiencies exceeding half a million theoretical plates are demonstrated for some compounds. Wider application and improved performance are anticipated with minimization of CZE band spread (due to adsorption and possibly other processes) and optimization of CZE buffers (for both the separation and their compatibility with electrospray ionization).

Capillary zone electrophoresis (CZE) is a form of free zone electrophoresis conducted in small-diameter capillaries and capable of ultrahigh resolution separations (*1*). CZE instrumentation is easily assembled, and separations obtaining more than 10^6 theoretical plates in less than 30 min have been demonstrated (*2–4*). Separations are based upon differences in the effective electrophoretic mobilities of analytes and do not include partitioning with a stationary phase, as in chromatography. Thus CZE provides high-resolution separations and selectivities which can be manipulated by changing the electrophoretic medium (i.e., typically pH and buffer composition). CZE is amenable to broad compound classes with application limited only by the necessity for solubility in the buffer and a nonzero net electrophoretic mobility. CZE is limited to small capillary diameters (generally ≤100 μm i.d.) to minimize convection due to the radial temperature gradient through the electrophoretic medium which results from Joule heating. This allows the high efficiencies obtainable, due to the nearly flat flow profile provided by electroosmosis, to be realized. Injection volumes for 100 μm i.d. capillaries are typically in the range of 5–50 nL, and electroosmotic injection methods allow simple, reproducible sample introduction with only minor contributions to band spread.

The major limitations of CZE are related to the sensitivity and range of application available with direct "on-column" detection methods (UV and fluorescence). Clearly, however, if detection limitations could be addressed CZE would provide a powerful analytical tool for a wide range of problems, particularly where only extremely small samples are available or where high separation efficiencies are required.

In a recent communication we described the first on-line combination of CZE with mass spectrometry (*5*), which also represented the first reported *direct* combination of any electrophoretic separation technique with mass spectrometry. This development was based upon the recognition that both ends of the CZE capillary did not have to be immersed in buffer reservoirs and provided a basis for new detection methods in which the electroosmotically induced flow could be analyzed at the column exit. The strong electroosmotic flow in CZE, which results from the substantial ζ potential of most suitable capillary surfaces, is sufficiently large under many conditions to result in elution of ions with both positive and negative electrophoretic mobilities. In our initial work it was shown that an electrospray could be produced at the capillary terminus, providing the basis for a viable CZE–MS interfacing method (*5*). Here we report details of the CZE–MS interface and describe new instrumentation and methods. The application of electrospray ionization (ESI) in CZE–MS is described, typical spectra and CZE–MS separations are presented, and current limitations related to both CZE and ESI are discussed. Future approaches to realizing the impressive potential of CZE–MS are briefly described.

EXPERIMENTAL SECTION

Instrumentation. The current instrumentation of CZE–MS is somewhat different from that first reported (*5*), as is shown in an overall schematic illustration in Figure 1. CZE is conducted by use of a fused silica capillary with automated electroosmotic sample introduction at the high voltage (+10 to 50 kV) anode. The voltage was provided by a Glassman High Voltage, Inc. (Whitehouse Station, NJ), Model LG60P2.5 0–60 kV dc power supply. The high-voltage region containing the buffer and sample containers is electrically isolated in an interlocked Plexiglas box. Untreated 100 μm i.d. fused silica capillaries were used for all studies. Operation of both the CZE and ESI processes requires an uninterrupted electrical contact for the electroosmotically eluting liquid at the capillary terminus. The electrical contact for the buffer at the low voltage (cathode) end of the capillary was made by silver from vapor deposition on the capillary and a supporting stainless steel sheath (which provided mechanical strength). This electrical contact also served to define the ESI voltage and was typically in the range of 3–5 kV. The focusing electrode was typically at +300 V, while the ion sampling nozzle and skimmer were at ground potential for the reported studies. Details of the CZE–MS interface are shown in Figure 2.

Several additional changes were made to the interface and mass spectrometer described previously (*5*) with the aim of improving the efficiency of ESI sampling and ion transmission. The ion focusing (radio frequency (rf) only) quadrupole chamber was differentially pumped with a specially designed Leybold Heraeus cryopump, consisting of a cylinder cooled to approximately 4 K, which enclosed the quadrupole and provided an effective pumping speed for N_2 of >30 000 L/s. The analyzer quadrupole chamber was pumped at 500 L/s with a turbomolecular pump. In this work a differentially pumped region between the nozzle and skimmer

[1] Present address: Du Pont, Savannah River Laboratory, Aiken, SC 29808

0003-2700/88/0360-0436$01.50/0

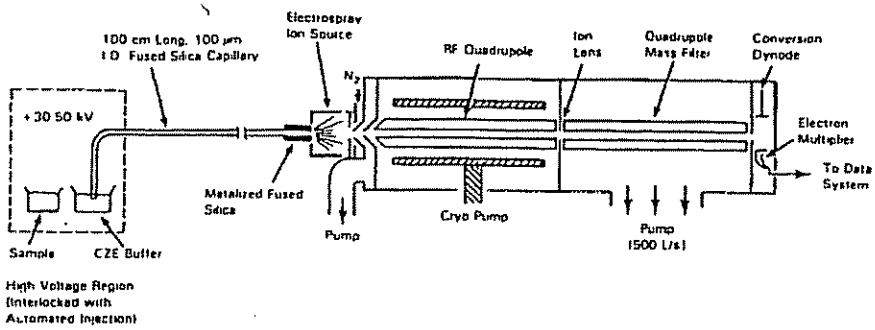

Figure 1. Schematic illustration of the CZE–MS instrumentation.

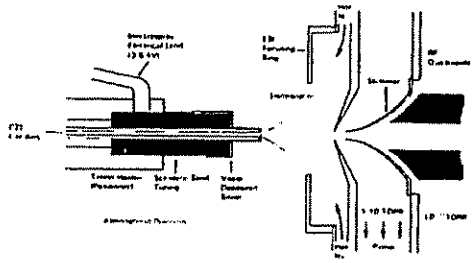

Figure 2. Detailed schematic of the electrospray ionization interface for CZE–MS (not to scale). The distance between the CZE capillary exit and the sampling nozzle is 1–2 cm.

was maintained at 1–10 Torr with a 150 L/s single-stage roots blower (Figure 1). The increased pumping speed allowed the orifice diameter of both the ion sampling nozzle and the skimmer to be increased to 1 mm. A single ion lens with an 0.64-cm aperture separated the ion focusing and analysis quadrupole chambers. The pressures in the two chambers were measured to be $\sim 1 \times 10^{-6}$ and 8×10^{-7} Torr, respectively. However, the high intensity of the molecular beam formed by the nozzle-skimmer inlet resulted in the actual pressure on the quadrupole axis being much greater in the first (ion focusing) quadrupole than that measured at the ion gauge (located outside the cryopump cylinder). The ion focusing quadrupole rods were machined so that they actually entered the throat of the skimmer (see Figure 2), with the aim of obtaining improved ion collection and transmission. The flow of N_2 (at ~70 °C) for desolvation of the electrospray was in the range of 3–6 L/min. The mass spectrometer (Extrel Co.) had a range of m/z 2000. The instrumentation for data acquisition and analysis has been described previously (5).

In addition to the CZE–MS instrumentation, a conventional CZE arrangement, with a fluorescence (McPherson FL-748 spectrofluorometer) or UV absorbance (ISCO V⁴) detector modified for on-column application, was used to evaluate electroosmotic injection procedures and to establish separation conditions. The detector cell length was ~0.8 mm for fluorescence and 1.0 mm for UV detection, corresponding to cell volumes of 6.3 and 7.9 nL, respectively. These studies also used untreated 100 μm i.d. fused silica capillaries and allowed a wider range of buffer compositions than the current CZE–MS interface but were restricted to the analysis of compounds with suitable fluorescence or UV absorbance.

RESULTS AND DISCUSSION

CZE Separations. To evaluate separation efficiencies obtainable by CZE, a mixture of dansylated amino acids was prepared at concentrations of $\sim 5 \times 10^{-6}$ M and analyzed using fluorescence detection (excitation at 310 nm with detection of emission at >320 nm). The injection utilized electroosmotic

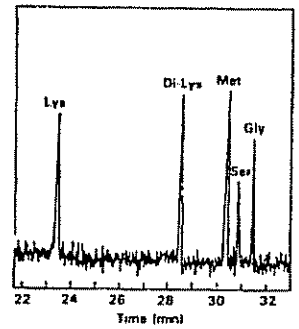

Figure 3. CZE separation at 30 kV of dansylated amino acids using florescence detection at pH 8.9 obtained by using a 2 m × 100 μm i.d. fused silica capillary

flow for 3 ± 0.15 s at 30 kV. The separation shown in Figure 3 was conducted in a 100 μm i.d., 200 cm long capillary (190 cm to detector) in a 10^{-2} M phosphate buffer at pH 8.92 with a 30-kV CZE voltage and a current of 9.2 μA. The electroosmotic flow coefficient was determined by the electromigration of 2-naphthol (which has a zero net electrophoretic mobility under these conditions) to be 7.88×10^{-4} cm²/V·s), resulting in an injection volume of 28 nL. The sample size injected for a specific mixture component depends upon the electrophoretic mobility and is therefore inversely proportional to the compounds' elution time (t_e). The injection sample size can therefore be calculated by using eq 1, where C is the

$$\text{sample size} = C v_c t_i V_i / t_e V_{CZE} \quad (1)$$

analyte concentration, v_c is the capillary volume (to the detector), t_i is the injection time, V_i is the injection voltage, and V_{CZE} is the separation voltage. Calculated sample sizes were thus in the range of 1–3 fmol for the four dansylated amino acids (glycine, serine, methionine, and lysine) and didansyllysine. Separation efficiencies ranged from approximately 3.3 $\times 10^5$ theoretical plates for lysine to 2.7×10^6 plates for glycine. These results demonstrate that high efficiency separations can be readily obtained by CZE; unfortunately, present restrictions on buffers for ESI and the positive ion mode of mass spectrometer operation prevented a direct transfer of these separations to CZE–MS.

Removal of the ground potential capillary exit from the buffer reservoir and use of the CZE–electrospray interface arrangement did not result in a substantial change in separation efficiencies for cases when a strong electroosmotic flow exists. This implied that a good electrical contact was maintained at the capillary exit and that the interface did not

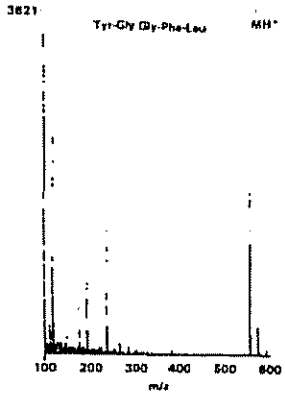

Figure 4. Electrospray ionization (ESI) mass spectrum of leucine enkephalin obtained by continuous electromigration introduction.

cause a significant loss of separation efficiency, due to the formation of a mixing volume or the induction of a significant component of laminar flow.

Operation of the Electrospray Ionization Interface. A key component of the CZE–MS interface is the provision for electrical contact of the buffer at the capillary exit. The ESI interface, shown in Figure 2, evolved from testing and evaluation of several designs aimed at providing the necessary electrical contact and minimizing dead volume. The lifetime of the capillary was typically limited to several days of operation before replacement was necessary; failure was usually attributed to loss of electrical contact at the capillary exit. It was also found desirable to deposit thick silver layers to extend capillary lifetime and to produce sufficient mechanical rigidity. The electrical contact was found to be excellent, and CZE–MS could be readily conducted at higher electroosmotic flows for a range of buffers.

As described in our recent communication (*5*), the ESI interface for CZE–MS is capable of achieving extremely low detection limits. The ESI process has been studied by Fenn and co-workers (*6–8*), but many questions remain concerning the nature of the field-assisted ion desorption process and other relevant concurrent processes. We have found that both analyte sensitivity and its mass spectrum depend not only on buffer composition and pH but also on the ESI voltage and ion focusing parameters. Indeed, selection of the CZE buffer often made a qualitative difference in sensitivity and sometimes precluded detection of certain analytes. Too low a N_2 flow also resulted in substantial contributions of water molecule adducts to the spectra of some compounds, as well as increased background and reduced sensitivities for many compounds. The mass spectra of larger compounds generally show increased contributions of multiply charged molecular ions. Detailed investigation of these parameters in the context of CZE–MS was beyond the scope of this work and will be the subject of future reports. For this work no attempt was made to optimize overall ESI performance, and the results should not be interpreted as representing optimum detection limits.

The ESI spectrum for leucine enkephalin, a pentapeptide of molecular weight 555, is shown in Figure 4. The mass spectrum was obtained by using 10^{-3} M ammonium acetate in 50% water/methanol solution during continuous electroosmotic injection through the capillary. The spectrum shows a dominant protonated molecular ion (m/z 556) and other contributions typical of the ESI method. Small contributions are also observed for $M(H_2O)H^+$, $M(H_2O)_2H^+$, and MNa^+, as well as larger contributions (*possibly* due to $M_2H_2ONa_2H_2^{3+}$) at m/z 236 and other multiply charged ions at m/z 264 and m/z 284. At this point all peak assignments must be considered tentative due to the limited resolution of the mass spectrometery (~800, 10% valley definition) and the limited experience with ESI.

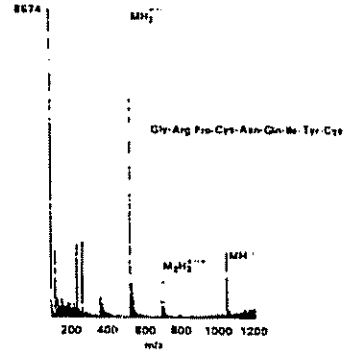

Figure 5. ESI mass spectrum of vasotocin.

The relative contributions of Na and H_2O adducts appear to be related to both the buffer composition and the degree of desolvation during ESI. Under some conditions, most importantly at high analyte concentrations, dimer species (M_2) can become significant. At low N_2 flows $M(H_2O)_nH^+$ ions dominate the spectra with smaller contributions due to $M_2(H_2O)_nH^+$, $M_3(H_2O)_nH_2^{2+}$, and $M_2(H_2O)_nH^{2+}$ (evident by smaller peaks evenly spaced between $M(H_2O)_nH^+$ peaks). In general, greater sensitivity and reproducibility appear to be obtained by using conditions which maximize desolvation and minimize cluster formation.

Figure 5 gives the ESI spectrum for vasotocin, a polypeptide of molecular weight 1050, which is representative of larger molecules studied to date. The mass spectrum shows the singly charged MH^+ ion but also the doubly charged ion (MH_2^{2+}) at m/z 526, the triply charged molecule at (MH_2OH^{3+}) at m/z 357, the triply charged dimer ($M_2H_3^{3+}$) at m/z 701, and sodium ion adducts ($MNaH_2^{2+}$ and $M_2NaH_2^{3+}$) at m/z 537.5 and m/z 708. The increasing signal, starting at m/z ~1000 is background due to rf noise pick-up by the detector preamplifier, which was subsequently eliminated. Additional peaks in the spectrum can possibly be attributed to other multiply charged protonated monomers or dimers with sodium or water ion adducts. Our results indicate that ESI mass spectra must be obtained under well-controlled conditions to be reproducible. These observations also suggest that peaks due to multiply charged ions could be useful in both the identification and detection (given an instrumentally limited m/z range) of higher molecular weight compounds.

Electroosmotic Injection for CZE–MS. Quantitative applications of CZE–MS will ultimately depend upon both the accuracy and precision of the sample injection step and the useful dynamic range of mass spectrometric detection. We have found electroosmotic sample injection to be generally attractive and to provide a simple, reproducible, and easily automated method for introduction of a relatively narrow sample band onto the CZE column. Figure 6 gives mass spectrometer response for three electroosmotic injections of a 10^{-4} M solution of trimethylphenylammonium iodide in a 50% water/methanol solvent. The trimethylphenylammonium ion was monitored at m/z 136 for injections of 5, 2.5, and 1 s, respectively, at 47 kV. As shown in Figure 6, both peak height and peak area correspond well to the length

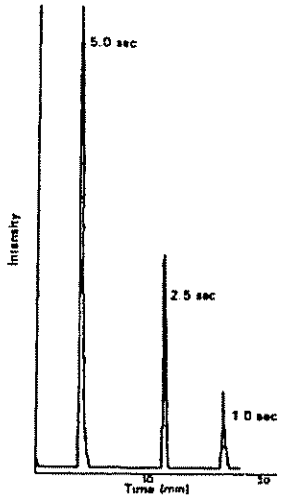

Figure 6. m/z 136 relative ion current for electroosmotic injection of trimethylphenylammonium iodide solution for three different injection times. Sample volume is directly proportional to injection time.

Table I Mixture Studied by CZE and CZE–MS[a]

compound	sample concn, mM/L	amt injected,[b] pmol	ion monitored (m/z)[c]	N[d]
1 thiamine	0.41	7.9	265	41 000
2. pyridoxamine	1.6	26	169	19 000
3 pyridoxine	1.2	18	170	7 800
4 tetrabutyl-ammonium hydroxide	0.05	0.6	242	620 000
5. cytidine	1.1	14	244	5 400
6 adenosine	1.3	13	268	15 000
7. L-phenylalanyl-L-phenylalanine	1.2	9.4	313	27 000
8 L-tryptopyl-L-phenylalanine	1.1	8.6	352	12 000

[a] By CZE–MS elution order (Figure 8). [b] Calculated by use of eq 1. [c] MH^+ ion in all cases except for the tetrabutylammonium cation. [d] From CZE–MS separations at pH 3 shown in Figures 8 and 9 calculated by using $N = 5.545(t_r/w_{1/2})^2$, where $w_{1/2}$ is the peak width at half height.

of the electroosmotic injection (eq 1), considering the uncertainity of ±0.15 s associated with the injection time. Improved injection precision can be obtained by using lower voltages for longer injection periods.

The peaks in Figure 6 have widths at half height in the range of 20–25 s and clearly display band spread contributions due to factors other than molecular diffusion. The addition of a small concentration of a salt, such as 10^{-4} M potassium iodide, resulted in a dramatic narrowing of the peak widths and allowed the higher efficiency separations reported in our initial communication (5) to be obtained. Higher ionic strength buffers led to even better separations, as shown later in this work.

CZE–MS Separations. An eight-component mixture described in Table I, containing one quarternary ammonium salt, was studied by CZE–MS in 10^{-2} M sodium phosphate buffers over a wide range of pH. The relative sensitivities and separation efficiences, and selectivities, were found to vary dramatically with pH. Figure 7 shows CZE separations of the

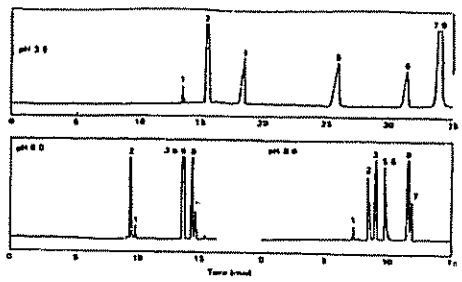

Figure 7. CZE separations at 30 kV using UV detection (at 215 nm) for the mixture given in Table I with three different pH buffer solutions. The separation used a 1.5 m long × 100 μm i.d. fused silica capillary.

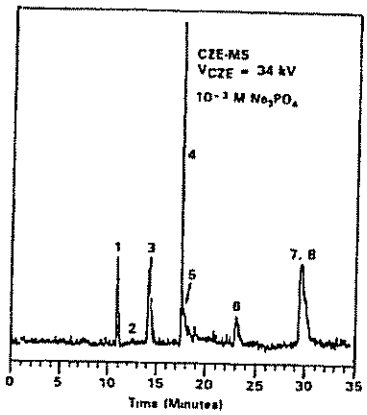

Figure 8. Reconstructured total ion electropherogram for the eight-component mixture given in Table I.

mixture as a function of pH in 10^{-2} M phosphate buffers obtained by using UV detection at 215 nm. (Note that the tetrabutylammonium salt is not detected.) The separation used a 30-kV gradient and detector located at the middle of a 1.5-m capillary. The efficiencies for most components are substantially less than feasible with CZE, probably due to adsorption on the fused silica capillary surfaces or sample overloading in the relatively low ionic strength buffer. The adsorption was also slightly dependent on the recent history of the capillary and was particularly evident at lower pH, resulting in less than optimum reproducibility from injection to injection. (In contrast, CZE separation times are often reproducible to <2%, with efficiencies similar to that shown in Figure 3 being typical.) The electroosmotic flow is smaller at low pH and both peak width and asymmetry are greater.

Figure 8 gives a CZE–MS electropherogram obtained from a separation at pH 3, in which 12 ions were monitored, including the eight listed for the test mixture in Table I. The separation used a 95-cm capillary and a 34-kV potential gradient. As in the CZE separations with UV detection at low pH (see Figure 7), relatively broad peaks are observed, indicating adsorption or sample overloading (which can cause band spread due to local perturbation of the electric field strength (1)). The background for each m/z value monitored was also substantial. The large background was apparently due to the residual material on the capillary surfaces from the mass spectrometer "tune-up" procedure which involved continuous electromigration introduction of the sample mixture prior to the analysis. Indeed, the "background" for each of

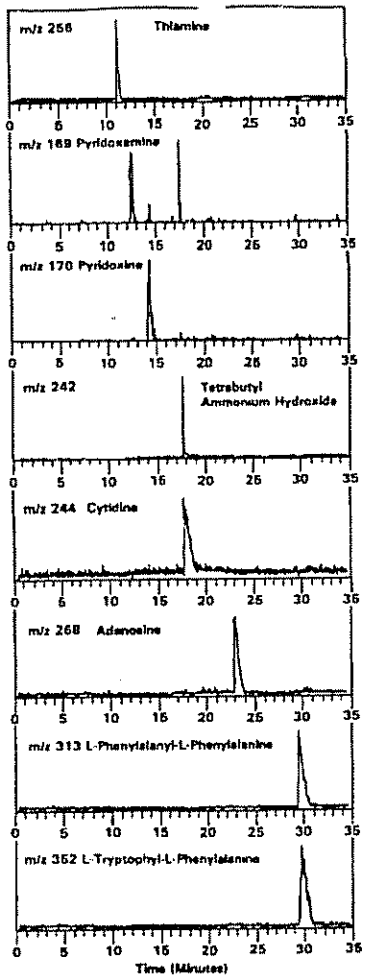

Figure 9. Single ion electropherograms for the eight-mixture component (see Figure 8).

the ions monitored was nearly 2 orders of magnitude greater than adjacent regions of the mass spectrum, implying that a reduction of adsorption on the capillary walls would lead to a substantial improvement in detection limits.

The concentration and injected sample size for each mixture component is given in Table I. The signal-to-noise ratios for the selected ion electropherograms for the eight mixture components given in Figure 9 range from approximately 30:1 to 100:1, suggesting detection limits are generally in the femtomolar range. Little effort was made to optimize the ESI and mass spectrometer performance in this study, and since detection limits were determined by chemical "noise" described above related to our "tune-up" procedure (as described above), we anticipate that substantially improved detection limits should be feasible. Comparison of Table I with Figure 9 also shows that there is a wide variation in the ion signal when the range of sample concentrations is considered. In terms of peak height per molar concentration, tetrabutylammonium hydroxide gave a response 10^3 greater than pyridoxamine with this buffer, although discrimination was not as extreme when considered in terms of peak area ($\sim 10^2$).

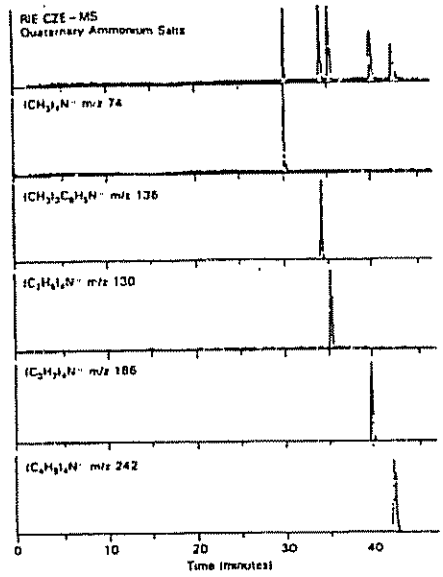

Figure 10. Total and single ion electropherograms for a quaternary ammonium salt mixture obtained by use of a 2 m × 100 μm i.d. capillary at 45 kV.

The compound specific contributions to band spread encountered with this mixture resulted in a wide variation of apparent separation efficiencies. Efficiencies, measured as numbers of theoretical plates (N), range from as low as 5400 for cytidine to 620 000 for the tetrabutylammonium ion and are listed for this separation in Table I. The peak width at half-height for the tetrabutylammonium ion was only 3.5 s. Obviously, either injection of smaller samples (or perhaps a larger buffer concentration in conjunction with a smaller CZE voltage) and the elimination of adsorption would improve both detection limits and the separation quality. Separations at higher pH (>9) gave greater efficiencies, but elution times became very similar and resolution was generally degraded.

The results in Figure 9 hint at the potential advantages of CZE–MS. In cases where adsorption degraded separations, efficiencies comparable to reported LC–MS results are obtained. For components not showing adsorption, efficiencies are obtained which far exceed those of conventional HPLC. Figure 10 shows the high efficiency of CZE–MS for a mixture of quaternary ammonium salts obtained in a 10^{-4} M phosphate buffer at pH 4 with a 2 m × 100 μm i.d. capillary at 40 kV. The figure shows the reconstructed ion electropherogram and single ion electropherograms for the five quaternary ammonium salts injected (4 s at 45 kV) as a 10^{-5} M solution. The separation efficiencies range from 160 000 theoretical plates for the tetrabutylammonium ion (m/z 242) to 330 000 theoretical plates for the trimethylphenylammonium ion (m/z 136). Injected sample sizes are approximately 300 fmol and signal to noise ratios are excellent. Our initial communication demonstrated attomolar detection limits for these compounds (5), and the present results indicate that such performance is feasible with substantially improved separation efficiencies.

CONCLUSIONS

Our research to date has shown CZE–MS to be a viable and potentially extremely useful new instrumental technique,

combining high separation efficiencies with selective and sensitive mass spectrometric detection. The electroosmotic injection process allows extremely small sample volumes (<10 nL) to be introduced for CZE–MS with negligible waste. Quantitation appears feasible and there is even the potential for obtaining useful structural information from the abundances of various multiply charged ions in the spectrum. The use of tandem mass spectrometry with CZE also offers an attractive method for compound identification.

Clearly, however, the ESI process needs to be well understood and controlled if reproducible results are to be obtained. Buffer composition, pH, desolvation gas flow, electric field strength, and even analyte concentration can be important variables for ESI mass spectra. Detection sensitivity varies greatly as well, and CZE buffers need to be selected with ESI efficiency taken into account. It is apparent that numerous options exist for manipulating ESI process, and the potential of CZE–MS will depend upon doing this in a useful manner.

The fact that CZE and ESI both use the same buffer imposes some restraints. Buffer concentrations of $\leq 10^{-2}$ M are generally required for ESI. In addition, more stable electrosprays are obtained for solutions containing organic solvents. Pure deionized water, for example, could not be effectively electrosprayed. While high ionic strength buffer concentrations are sometimes desired in CZE to either help minimize adsorption or reduce local perturbations of the electric field strength caused by high sample concentrations, such conditions can require lower voltages (and longer separation times) if separation efficiency is not to be degraded due to excessive heat generation.

Our initial CZE–MS work has involved separations in untreated fused silica capillaries and electrospray ionization in the positive ion mode, which has limited the range of analytes studied to date. Untreated fused silica capillaries have a net negative surface charge that results in electroosmotic flow from the high-voltage anode toward the (low-voltage) electrospray cathode. The production of positive ions during ESI is enhanced by use of a low pH buffer. However, low pH buffers with unmodified fused silica capillaries reduce the bulk electroosmotic flow which can cause instability in the electrospray (and can even affect CZE–MS separations). In addition, adsorption of neutral species or positive ions on the negatively charged surfaces of the fused silica capillaries can cause a dramatic loss of separation efficiency.

Two options exist for removing these limitations. First, operation in an ESI negative ion mode, as demonstrated by Fenn and co-workers (7), would clearly broaden application. This is an attractive alternative since recent work has shown that adsorption of proteins (which pose some of the greatest adsorption difficulties) during CZE can be largely eliminated by inducing negative charges on both the analyte and the CZE capillary surface (2). Other alternatives involve deactivation of the sites on fused silica capillaries resulting in adsorption (1) and even modification of surfaces to create a net positive charge (which would require reversal of the polarity of the CZE voltage). Finally, efficiencies well in excess of 10^6 theoretical plates are clearly possible with CZE–MS by using smaller diameter capillaries and higher electric field strengths. These and other approaches to the extention and optimization of CZE–MS are currently being investigated.

ACKNOWLEDGMENT

We thank H. T. Kalinoski for contributions to this work.

Registry No. Thiamine, 59-43-8; pyridoxamine, 85-87-0; pyrioxine, 65-23-6; tetrabutylammonium hydroxide, 2052-49-5; cytidine, 65-46-3; adenosine, 58-61-7; L-phenylalanyl-L-phenylalanine, 2577-40-4; L-tryptophyl-L-phenylalanine, 6686-02-8; tetramethylammonium, 51-92-3; trimethylphenylammonium, 3425-74-2; tetraethylammonium, 66-40-0; tetrapropylammonium, 13010-31-6; leucine enkephalin, 58822-25-6; vasotocin, 9034-50-8.

LITERATURE CITED

(1) Jorgenson, J. W.; Lukacs, K. D. *Science* **1984**, *222*, 266.
(2) Lauer, H. H.; McManigill, D. *Anal. Chem.* **1986**, *58*, 166.
(3) Jorgenson, J. W.; Lukacs, K. D. *Anal. Chem.* **1981**, *53*, 1298.
(4) Green, J. S.; Jorgenson, J. W. *J. Chromatogr.* **1988**, *352*, 337.
(5) Olivares, J. A.; Nguyen, N. T.; Yonker, C. R.; Smith, R. D. *Anal. Chem.* **1987**, *59*, 1230.
(6) Yamashita, M.; Fenn, J. B. *J. Phys. Chem.* **1984**, *88*, 4451.
(7) Yamashita, M.; Fenn, J. B. *J. Phys. Chem.* **1984**, *88*, 4671.
(8) Whitehouse, C. M.; Dreyer, R. N.; Yamashita, M.; Fenn, J. B. *Anal. Chem.* **1985**, *57*, 675.

RECEIVED for review July 1, 1987. Accepted October 25, 1987. We thank the U.S. Department of Energy, Office of Health and Environmental Research, through Contract DE-AC06-76RLO 1830 for support of this work. Pacific Northwest Laboratory is operated by Battelle Memorial Institute.

ing terms in the energy expression involving both the core and valence orbitals have the form

$$\langle\mu|\Sigma_j(2J_j-K_j)|\nu\rangle\,. \tag{A.8}$$

where μ and ν are functions belonging to the valence space, i.e., the space orthogonal to the set (A.4)

Thus in the many-electron space satisfying (A.7), the variational wavefunction Φ_{val} can be obtained by solving for the optimum wavefunction of the form

$$a(\Phi_{val}) \tag{A.9}$$

using the $N' = N - 2q$ electron hamiltonian

$$\mathcal{H} = \sum_i^{N'} h^{core}(i) + \sum_{i>j}^{N'} 1/r_{ij}\,. \tag{A.10}$$

where $h^{core}(i)$ is given by (A.3) The only restriction made here is that the core orbitals are not reoptimized to reflect changes in the valence orbitals

However, given the Φ_{core} the use of (A.9) and (A.10) involves no additional approximations, $h^{core}(i)$ includes all the proper terms that arise from the Pauli principle. The major advantage of the above procedure is that the two-electron integrals involving the core orbitals are processed only once to form the matrices

$$\langle\mu|h^{core}|\nu\rangle$$

With these matrices one can carry out various types of calculations (HF, GVB, CI) on the various excited states while working with only a small number of electrons, two in the case of ethylene and allyl cation. In this case the calculations take no longer than if only two electrons had been present

The h^{core} forms an effective potential for movement of the valence electrons This differs from the various pseudopotential methods and usual effective potential methods in that we do *not* approximate the way that the field terms due to Φ^{core} enter the wave function.

References

[1] W A Goddard III, T H Dunning Jr., P J Hay and W.J. Hunt, Accts Chem Res 6 (1973) 368
[2] D.L. Huestis and W.A. Goddard III, Chem. Phys. Letters 16 (1972) 137, see also R.C Morrison and G.A Gallup, J Chem Phys 50 (1969) 1214
[3] D L Huestis, Ph D Thesis, Calif Inst of Tech. (Sept 1972)
[4] S L Guberman and W A. Goddard III, Chem Phys Letters 14 (1972) 460.
[5] S L Guberman, Ph D Thesis, Calif Inst of Tech. (Nov. 1972)
[6] T H. Dunning, Ph.D Thesis, Calif. Inst of Tech. (Sept. 1969)
[7] S. Huzinaga, J. Chem Phys 42 (1965) 1293.
[8] T H Dunning Jr., J Chem Phys. 53 (1970) 2823
[9] T.H Dunning Jr., W J Hunt and W A Goddard III, Chem Phys Letters 4 (1969) 147.
[10] C.B Bender, T H Dunning, H F Schaefer III, W.A Goddard III and W J Hunt, Chem Phys. Letters 15 (1972) 171.
[11] W J. Hunt, W.A Goddard III and T H Dunning Jr., Chem. Phys Letters, to be published.
[12] W J Hunt, Ph.D Thesis, Calif Inst of Tech. (Sept.) 1971).
[13] S.D. Peyerimhoff and R J Buenker, J. Chem. Phys 15 (1969 2518

CHEMICAL PHYSICS 4 (1974) 417–427. © NORTH-HOLLAND PUBLISHING COMPANY

INTEGRAL CROSS SECTIONS FOR ION–MOLECULE REACTIONS. I. THE GUIDED BEAM TECHNIQUE

E. TELOY and D GERLICH

Fakultät für Physik der Universität Freiburg i. Br., Germany

Received 19 March 1974

A technique is described, that allows the measurement of integral cross sections for ion–molecule reactions and electron-transfer processes in the energy range from typically 0.1 to 20 eV (lab). Basically similar to the tandem mass spectrometer method, it uses inhomogeneous oscillatory electric fields for the storage and guidance of the primary ions and for the collection of the secondary ions. By these means a reduction of the number of excited ions in the primary beam and a good definition of the kinetic energy are obtained, together with a collection and detection probability for the secondary ions, that approaches unity for all scattering angles in a broad energy band. This ion beam intensity (10^5 to 10^7 ions per second) is only weakly dependent on the kinetic energy down to typically 0.15 eV (lab) The distribution of the collision energies is mainly determined by the thermal motion of the reactant gas in the scattering chamber ($T = 300$ K) Measurements are reported for the reactions $Ar^+ + D_2 \rightarrow ArD^+ + D$ and $Ne^+ + CO \rightarrow C^+ + Ne + O$.

1. Introduction

The current interest in ion–molecule reactions comes mainly from two separate origins. First, reaction rates and cross sections provide useful data for the quantitative understanding of processes in plasmas (in the widest sense, e.g., the high atmosphere) Second, one can expect to get general insight into the dynamics of chemical reactions from such studies For the latter purpose, accurate measurements of integral cross sections in the energy region, where the collision energy is comparable to chemical binding energies, are of particular significance.

One of the best established techniques for measurements in this region is the tandem mass spectrometer method, where a beam of mass-selected ions collides with a low pressure neutral gas in a scattering chamber, and the ionic products are analyzed in a second mass spectrometer [1–9] Besides its merits, this technique in its present form still has several disadvantages. Some of them are:

(1) The preparation of an ion beam with sufficient and stable intensity, well defined energy and good directionality is – at low energies – impeded by space charge effects and the influence of spurious electric and magnetic fields.

(2) The energy of the beam in the collision region can be influenced to an unknown extent by differences of the work function of the metal surfaces.

(3) If the primary ions are produced by electron impact, the beam may contain ions in metastable electronic states, and, in the case of molecular ions, in excited vibrational and rotational states. This is usually undesired and can generally be circumvented only at the expense of intensity

(4) In general, the collection and detection probabilities for the secondary ions are not independent of their mass, energy, scattering angle, nor of the position in the scattering region where they have been formed The collection probability can be improved by applying an electrostatic field to the scattering region, but the distribution of collision energies will spread simultaneously. This difficulty is reflected by the fact, that two versions of tandem mass spectrometers are used, the longitudinal and the transverse type, which show optimum collection efficiencies for fast ions, scattered in forward direction, or for slow ions (as produced by electron transfer), which can be collected sideways by

weak fields, respectively.

Thus paper shows that these problems can to a great extent be overcome by utilizing inhomogeneous oscillatory electric fields for the storage, guidance, and collection of the ions. A brief account of the properties of such fields is given in section 2.

Section 3 describes how these principles are used in our scattering apparatus; section 4 gives an account of the measuring procedure and of the tests performed to assess the proper function of the machine. In section 5 cross sections of the reactions

$$Ar^+ + D_2 \rightarrow ArD^+ + D, \quad (1)$$

and

$$Ne^+ + CO \rightarrow C^+ + O + Ne \quad (2)$$

are presented. Further experiments will be reported in a subsequent paper.

2. Ions in inhomogeneous oscillatory electric fields

A distinctive feature of our apparatus (fig. 1) is the application of inhomogeneous oscillatory electric fields for ion optics at three different points: the ion source, the mass filter, and the octopole beam guide. A brief discussion of the motion of ions in such fields is given here; a more detailed study will be published elsewhere.

Two well known examples for the use of such fields are the quadrupole mass filter [10, 13] and the quadrupole ion trap [11–13]. The usual analytic treatment of the ion motion in these arrangements is applicable only to a few very special geometrical shapes of the electric field. For inhomogeneous fields in general, approximative treatments have been given [14, 15].

The equation of motion is

$$m\mathrm{d}^2\mathbf{r}/\mathrm{d}t^2 = q\mathbf{E}_0(\mathbf{r})\cos(\omega t + \varphi) + q\,\mathbf{E}_s(\mathbf{r}), \quad (3)$$

where m and q are mass and charge, $\mathbf{r}$ and t position and time, $\mathbf{E}_0$ is the amplitude of the oscillating part of the field and $\mathbf{E}_s$ the static part, $\nu = \omega/2\pi$ is the frequency and φ an arbitrary phase constant. We intend an approximate solution of the form

$$\mathbf{r}(t) = \mathbf{r}_0(t) + \mathbf{R}(\mathbf{r}_0, t), \quad (4)$$

where the trajectory $\mathbf{r}(t)$ is composed of a smooth part $\mathbf{r}_0(t)$, which does not depend on φ, and an oscillatory part $\mathbf{R}$, which becomes zero when averaged over all possible values of $\omega t + \varphi \leq \pi$.

As a first-order approximation, we obtain

$$\mathbf{R} = q\mathbf{E}_0(\mathbf{r}_0)\cos(\omega t + \varphi)/m\omega^2 \quad (5)$$

and a differential equation for $\mathbf{r}_0$

$$m\mathrm{d}^2\mathbf{r}_0/\mathrm{d}t^2 = q^2\nabla_0\mathbf{E}_0^2(\mathbf{r}_0)/4m\omega^2 + q\mathbf{E}_s(\mathbf{r}_0), \quad (6)$$

∇_0 acting with respect to $\mathbf{r}_0$. An effective (ponderomotive) potential ψ^* can be defined by

$$\psi^*(\mathbf{r}_0) = q^2\mathbf{E}_0^2(\mathbf{r}_0)/4m\omega^2 + q\phi_s(\mathbf{r}_0), \quad (7)$$

where ϕ_s is the electrostatic potential, that belongs to $\mathbf{E}_s$:

$$\mathbf{E}_s = -\nabla\phi_s. \quad (8)$$

For a derivation of (7) see [14, 15]. The smooth trajectories can then be derived from ψ^* in analogy to an ordinary potential:

$$m\mathrm{d}^2\mathbf{r}_0/\mathrm{d}t^2 = -\nabla_0\psi^*(\mathbf{r}_0). \quad (9)$$

In general, this equation of motion can be solved much easier than the original one, since it does not contain the time explicitly. With $\mathbf{r}_0(t)$ known, $\mathbf{R}(t)$ and an approximate $\mathbf{r}(t)$ can be computed. But for many applications, the effective potential will give a sufficient idea of the ion motion by itself.

This approximation becomes exact in the limit $\omega \rightarrow \infty$, even when $|E_0|$ is increased proportionally to ω. As a rule, the approximation remains good, when ω is chosen high enough, so that the conditions

$$q|\nabla_0 E_0^2|/m\omega^2|E_0| \leq 0.3, \quad (10)$$

and

$$|(\mathrm{d}\varphi/\mathrm{d}t)\nabla_0|E_0|/\omega|E_0| \ll 1 \quad (11)$$

are satisfied along the path of the ions. The latter restriction may be disregarded at places where the oscillatory field is too weak as to influence the ion motion markedly, e.g., near the axis of an octopole (see below).

The first, essential term of ψ^* (7) depends on the mass and the charge of the ion, but not on the sign of the charge. For the present applications, its most important property is, that fields can be found, which show absolute maxima of ψ^* in two or three dimensions of space and therefore are able to guide or to trap ions. The quadrupole mass filter and the ion trap are well known examples, with the additional (most important) possibility of high resolution mass selective modes of operation. But in these properties are not required, one is free to adapt the geometrical shape to special experimental needs. For instance, ion traps can be constructed, in which a nearly field-free volume is enclosed by steep repulsive walls of the effective potential. Such a well can be formed by an arrangement of equally spaced parallel rods, which are concentrically to rf voltages of opposite phase, or similarly by metal plates or wires.

Fig. 1. Simplified scheme of the apparatus (not to scale). (1a, b) Gas inlet for ion source and scattering chamber, (2a–b) to cold trap and mercury diffusion pumps, (3) storage ion source, (4) cathode and electron beam, (5) electrodes for charging and pulsing of the ion beam, (6) rf mass and velocity filter (8 cm long, 1 cm diameter, 0.32 cm), (7) rf octopole (31.7 cm long, few diameter, 0.32 cm), (8) scattering chamber (effective length 9.1 cm), (9) ionization gauge, (10) capacitance manometer (MKS Baratron Type 90), (11) electrode for the scattering chamber, operated by an electrometer, (12) acceleration lens, (13) lenses for the steering of the ion beam; (14) entrance slit of the mass spectrometer (0.15 × 1.6 cm), (15) metal box, defining an electrical potential to the mass spectrometer (~3 kV), (16) poles of the 90° magnet (radius 12.5 cm), (17) exit slit (0.3 × 1.4 cm), (18) voltage feed-through and counter (~30 kV), (19) scintillator (Nuclear Enterprises NE 160) and quartz window, (20) photomultiplier (Valvo XP 1910).

ions leaving the source will in general have a narrow energy distribution and most of them will be in the electronic ground state. For molecular ions, a nearly thermal distribution of the vibrational and rotational states is expected. If ion–molecule reactions occur, the products are contained in the ion yield. In some cases, this allows experiments with ion species which otherwise are difficult to produce, in other cases, especially if one of the reactants is an impurity, the new species are unwanted and must be suppressed in the next stage of the apparatus.

Fig. 2 shows the electrode arrangement of the source. It consists of 8 nearly identical molybdenum

Fig. 2. Electrode arrangement of the storage ion source (simplified). The upper half, that is essentially symmetric with respect to the central plane c, has been omitted. End plates (e) have also to the electron beam instead of U holes)

plates, in which U-shaped holes are cut, and 2 solid end plates. Three of the central plates have an outlet for the ions. An rf voltage is connected alternately to the plates. A positive dc voltage (with respect to the mean potential of the rf plates) is applied to the end plates, repelling positive ions. The electron beam goes through one leg of the U hole, the ion outlet is at the end of the other leg. All ions, that leave the source must have migrated along the U path. Metastable neutral species, which are formed in the electron beam, cannot leave the source without colliding with a surface.

Collisions with molecules occurring in regions with a strong oscillatory field may, depending on the rf phase, enhance the mean kinetic energy of the involved ion, even if the momentary kinetic energy is lowered in the collision process, and in consequence cause the loss of that ion. Therefore, it is important that the ions move in a weak field most of the time and have only short encounters with the repulsive rf walls. This requirement is met by applying a high number of rf electrodes whose fields compensate mutually in most of the storage volume. Rather than being extracted ions are allowed to leave through the outlet, an opening in the rf walls. Typical operating conditions for this source are: pressure 10^{-2} torr, frequency 10 MHz; rf amplitude 30 to 200 V, dc voltage at the end plates +1 V, electron current 10 μA. With rf power switched off, virtually no ions leave the source.

The kinetic energy distribution of the ions leaving the source depends on the gas composition, the pressure, and other parameters. For Ne^+ and Ar^+, 0.1 eV fwhm can be obtained. For N^+ from N_2, which often is formed with excess kinetic energy, 0.2 eV has been measured. Typical average storage times are from 0.1 to 1 ms (in the continuous mode of operation). During our experiments the ion current was limited to 10^{-12} A in order to avoid excessive dead-time losses in the detector-counter. But it is estimated that 10^{-9} A can be obtained under favorable conditions without considerable spread of the energy distribution.

The energy distribution and the residual fraction of excited ions can be further improved using pulse techniques. Ions are formed by a short electron pulse while the ion outlet is closed by a positive dc potential at a nearby electrode. Several milliseconds later, the stored ions are discharged by lowering this potential.

Measured cross sections of several reactions, for instance

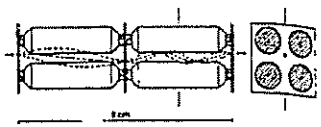

Fig. 3. Mass and velocity filter, longitudinal and transverse cross sections. "Smooth" trajectories for passing ions are indicated by broken lines as 1st and 3rd order trajectories in the 1st and 2nd stage respectively. Actually, trajectories have the same order in both stages.

$$N^+ + CO \rightarrow C^+ + NO,$$

and

$$H_3^+ + He \rightarrow HeH^+ + H_2,$$

have been found to depend strongly on the storage time and the pressure in the source. This is evidence for the de-excitation of metastable electronic and vibrational states during storage.

The main purpose of the combined *mass and velocity filter* (fig. 3) is to separate the desired ion species from other ones that may have been produced in the ion source. For this task, a moderate or poor mass resolution is frequently sufficient. The present construction has been employed to circumvent the necessity for the elaborate system of accelerating and decelerating lenses before and behind the mass-selecting device, that sometimes is the cause of considerable ion losses at low energies. The kinetic energy of the ions in the filter is usually between 0.5 and 1 eV. It consists of two quadrupoles arranged in series, similar to conventional "mass filters"; but in contrast to these, mass selection is not effected by stability or instability of the ion trajectories. Instead, we have used the properties of the effective potential, eq. (7), to devise lenses with a mass-dependent focal length (which is impossible with static electric fields).

Ions that pass through the circular entrance hole, are focused onto a hole in the central plate and in turn onto a hole in the exit plate. The 3 holes are transposed radially with respect to the quadrupole axis. There are two operational modes: first order, where the 3 nodes of the trajectories are situated at the 3 holes, and third order, where 4 additional nodes exist. When operated

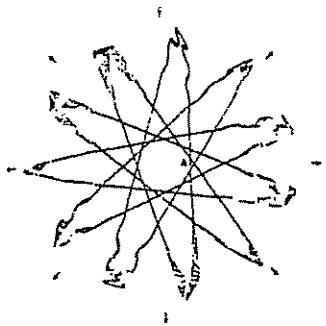

Fig. 4. Ion trajectories in an oscillatory octopole field, projected parallel to the axis. The position of the poles is indicated by arrows. Simple ions have the same mass, starting position (A) and initial transverse momentum, but different phases with respect to the oscillatory field. Trajectories have been calculated by stepwise integration, not by using the approximation, that is described in the text.

in the third order mode, mass and velocity resolution of the filter are improved at the expense of the transmitted intensity.

At the exit, the ions pass through a little tube (0.6 cm long, 0.1 cm inner diameter), that serves as a collimator for their injection into the adjacent octopole, and is the only leak between the two separately pumped vacuum chambers.

An *rf octopole* is used to guide the primary ions through the scattering chamber, to collect the secondary ions and to guide them to the mass spectrometer together with those primary ions that have not reacted. It consists of 8 parallel cylindrical rods which are equally spaced in an octogonal array. Neighbouring poles are connected to opposite phases of the rf voltage. The effective potential is proportional to the sixth power of the distance from the central axis. Fig. 4 shows several ion trajectories in such a field, simulated by a computer. Since the longitudinal velocity of the ions is not influenced by the rf field, their motion is

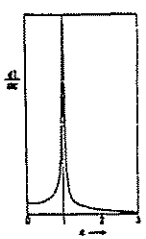

Fig. 5. Influence of the oscillatory octopole field on the kinetic energies of ions. The graph, result of a Monte-Carlo calculation, shows the distribution of ε, defined as the instantaneous value of the kinetic energy of the transverse motion divided by its initial value, in the time-average. The longitudinal kinetic energy, which is prevailing by *far* for primary ions, is not influenced by the field. Ion trajectories have been simulated starting near the axis of the octopole.

like a series of specular reflections in a cylindrical tube, its diameter slightly depending on the mass and energy.

Again, preference has been given to a multipole over a quadrupole configuration, because the oscillatory field is weak in a larger portion of its tubular volume. By these means the influence of the rf field on the distribution of the kinetic energy is reduced (see below) and the fringe fields at both ends have comparatively little effect.

The collimating entrance tube permits maximum angles of 10° with respect to the axis. The primary ions are accelerated or decelerated to the desired kinetic energy by a voltage between the tube and the average potential of the octopole. The dc component of the field in the vicinity of the end of the tube is nearly spherically symmetric and therefore has little influence on the angular distribution of the ions.

During the interaction with the oscillatory field, the kinetic energy is momentarily changed, and therefore the distribution of the collision energies is influenced to some extent. To estimate this influence, the kinetic energy is divided up into a longitudinal and a transverse part. Only the transverse part undergoes temporary changes. Its time-averaged distribution is shown in fig. 5. For ions with an initial angle of 10°, the initial

transverse part of the kinetic energy is less than 3% of the total, and the total energy varies from 97% to 106%, but peaks near 100%.

Since the primary ions are guided through the scattering chamber by the octopole, all secondary ions formed as the product of collisions with the target gas, have their origin within the guiding field. Provided the effective potential is high enough, they cannot escape. Generally, most of them are directed forward, according to the center-of-mass motion. Backward-moving ions will – in most cases – be reflected at the ingestion end of the octopole by the potential of the collimating tube and the end plate of the mass filter. Only at low primary energies, this potential may be too low and ions be lost. This can be avoided by a pulsed mode of operation. A sequence of short ion pulses is injected into the octopole, and the potential of the mass filter is raised immediately after each pulse so that all backward-running ions are reflected.

Mass spectrometer and detector. A perfect mass selector–detector combination would produce exactly one counting pulse for every ion of a given mass, that leaves the octopole, irrespective (in wide limits) of kinetic energy and direction of motion. We have tried to approximate this ideal by (1) choosing a comparatively large magnetic mass spectrometer with wide slits and a high operating voltage (3 kV), which therefore accepts and transmits incoming ions from a large volume of phase space, (2) choosing a scintillation detector [16, 17] that accepts all the phase space that is transmitted by the mass spectrometer, (3) matching the phase space of the ions that leave the octopole, to the phase space that is accepted by the mass spectrometer. This is done by a series of lenses between the end of the octopole and the entrance slit.

The degree to which the above requirements for perfect operation can be met, depends on the reaction cross section, that is actually measured and can only be inferred from indirect evidence, e.g., the charge balance (see section 4) and the pulse-height distribution of the photomultiplier pulses. We estimate that under normal conditions at least 95% of all ions produce a counting pulse.

The pulses are further processed by gating and counting circuits which produce automatically the measurement cycles described in the following section, punch the raw data into paper tape, and change the acceleration voltage for the next cycle.

4 Measuring procedure and functional tests

During the measurements, a constant flow of scattering gas is admitted into the scattering chamber. A vent in the wall of the chamber is opened and closed alternatively for one counting period, changing the inside pressure by more than a factor of ten. By this procedure the background pressure outside the chamber is virtually constant. When the vent is closed, the pressure profile along the axis of the octopole has a nearly trapezoidal shape. The pressure difference between inside and outside is measured by a capacitance manometer (MKS Baratron Type 90), a typical reading is 1.5×10^{-4} torr in the closed state. Primary and secondary ions are counted for periods of typically 10 s, both in the closed and open state, and the results are corrected for dead-time losses in the counter. A cross section $\bar{\sigma}$, that has still to undergo further corrections, is computed by the formula

$$\bar{\sigma} = 2kT_2(N_{2c} - N_{2o})/(N_{1c} + N_{1o})L(P_c - P_o). \quad (12)$$

where the N's denote corrected counting rates for primary and secondary ions in the closed and open states (subscripts 1, 2, c, o), L is the effective length of the scattering chamber, the P's are pressure differences, k and T_2 are Boltzmann's constant and absolute temperature. The expression $\frac{1}{2}(N_{1c} + N_{1o})$ in the denominator corrects for loss of primary intensity in the scattering chamber.

The average kinetic energy of the primary ions and its approximate distribution is determined in two different ways. (1) By observing the primary intensity, while the dc-potential of the octopole is changed gradually from positive to negative values. The potential for which the intensity is 50% of its saturation level is taken as the zero-point of the energy scale. (2) By using the pulsed mode and determining the kinetic energy by a time-of-flight method (see fig. 6). Both methods yield values for the energy and its spread, that are in good agreement. Typical energy spreads are from 0.06 to 0.2 eV fwhm. This means, that in most cases the distribution of the collision energies is essentially determined by the thermal motion of the scattering gas [18–20], and the primary energy spread can be neglected.

To assess the proper function of the apparatus, several tests are performed on a routine basis:

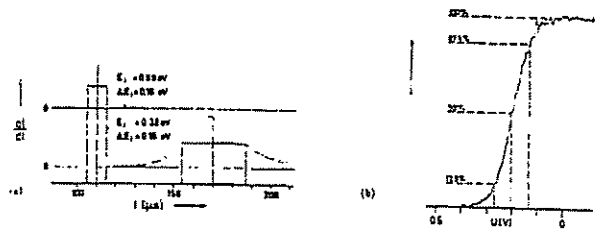

Fig. 6. The kinetic energy of the primary ions and its spread is determined in two independent ways: (a) The time-of-flight distribution is registered for short ion pulses by a fast multichannel scaler, with a resolution down to 100 nsec [33]. High energy ions, whose time-of-flight can be calculated, are used to establish the origin of the time-scale. (b) Retarding potential method. The intensity I of the primary ion beam is measured, while the dc potential U of the octopole (with respect to the source potential) is changed. The potential at 50% of the saturation level is taken as the origin of the energy scale. The spread corresponds to the potential difference between the 12.5% and 87.5% levels. Both methods yield essentially equal results. Examples are for N^+.

(1) Registration of the mass spectrum for the primary and secondary ions. In this way, impurities in the gases are detected by electron-transfer processes or by reactions.

(2) Observation of the peak form for primary and secondary ions. Perfect adjustment of the ion lenses and the detector is confirmed when the peaks have a trapezoidal shape, with sharp edges.

(3) Establishing the independence of the counting rates (in wide limits) on detector voltage, photomultiplier voltage, and threshold setting of the pulse-height discriminator.

(4) Checking the independence of the apparent cross section (as given by the above formula) on combined variations of the pressure in the source chamber and the storage time and thereby on variations of the mean number of collisions, which the primary ions undergo in the source. If excited species are present in the primary beam and have an appreciably different cross section, a dependence of the apparent cross section on the mean number of collisions is expected (and has been found in certain cases).

(5) The apparent cross section should be independent (in wide limits) of the rf voltage of the octopole, of the pressure in the scattering chamber (test for errors induced by secondary collisions) and of the primary intensity (test for the correct compensation of the counting losses).

(6) If the number of the positive ions is conserved for all competing processes that occur in the system under investigation, the sum of the counting rates for all relevant ion masses should be independent of the pressure in the scattering chamber. Or, to state it in another way, the apparent cross section for the loss of primary ions, given by

$$\bar{\sigma}_i = -2kT_2(N_{1c} - N_{1o})/(N_{1c} + N_{1o})L(P_c - P_o) \quad (13)$$

should be equal to the sum of all apparent cross sections, that produce secondary ions.

This represents a good overall test for proper ion collection, transmission and detection. Typical deviations from perfect balance are less than 5% of $\bar{\sigma}_i$ for many reactions. It may be useful to remark, that a fair balance could be reached only, after the open electron multiplier, that had been used for ion detection earlier, was replaced by a scintillation detector.

When all tests produce good results, the remaining systematic error of the cross section is estimated to be generally less than ± 15%, at very low energies (E_i < 0.5 eV) perhaps somewhat larger. The main uncertainties are: the absolute value of the pressure and its profile in the octopole, the path length of the primary ions; the influence of elastic collisions and secondary reactions; the differences in the detection probabilities for primary and secondary ions.

5. Measurements and discussion

For several ion–molecule reactions and electron-transfer processes cross sections have been obtained, that allow a comparison with results from other workers. Two examples are given here.

The reaction $Ar^+ + D_2 \rightarrow ArD^+ + D$, together with its isotopic variant $Ar^+ + H_2$, is one of the most thoroughly studied. Because of the favorable mass ratio of the colliding particles nearly thermal collision energies are accessible with tandem mass spectrometers. Thus is the energy region, where the polarization model by Langevin, Gioumousis and Stevenson [21, 22], if ever, is expected to give satisfactory predictions.

At low collision energies, a careful distinction must be made between the true cross section σ and the measured, or effective, cross section $\bar{\sigma}$, that results from the averaging due to the thermal motion of the scattering gas [18–20]

$$\bar{\sigma}(v_1) = \int_0^\infty (g/v_1)\,\sigma(g)\,f^*(g,v_1,T_2)\,dg, \qquad (14)$$

where

$$f^*(g,v_1,T_2) = \sqrt{m_2/2\pi kT_2}\;(g/v_1) \times \{\exp[-(m_2/2kT_2)(g-v_1)^2] - \exp[-(m_2/2kT_2)(g+v_1)^2]\} \qquad (15)$$

is the generalized Maxwell–Boltzmann distribution that describes the relative velocities g for a fixed velocity v_1 of the primary ions. Here, m_2 is the mass and T_2 the temperature of the scattering gas molecules, m_2 the mass of the primary ions, further, μ is the reduced mass, $E_1 = \frac{1}{2}m_1v_1^2$ the primary, or laboratory, kinetic energy and $E = \frac{1}{2}\mu g^2$ the collision energy. For $T_2 \rightarrow 0$ we have $g \rightarrow v_1$, $E \rightarrow E_1\mu/m_1$ and $\bar{\sigma}(v_1) \rightarrow \sigma(g)$. At low energies, i.e., if $v_1 \ll \bar{v}_2$, [$\bar{v}_2 = (8kT/\pi m_2)^{1/2}$ being the mean thermal velocity] f^* becomes nearly independent of v_1 and $\bar{\sigma}$ is therefore mainly proportional to the time of traversal of the primary ions through the scattering chamber, L/v_1, irrespective of the functional dependence of $\sigma(g)$. To facilitate the presentation and discussion of the data, reaction rate constants for the above distribution f^*, $K^*(v_1) = \bar{\sigma}(v_1)v_1$, are preferred rather than cross sections $\bar{\sigma}$. For

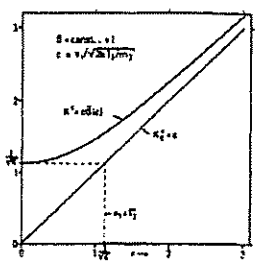

Fig. 7. Influence of the thermal motion on the measured rate constant K^*. The example shows K^*, defined for the generalized Maxwell–Boltzmann distribution $f^*(g,v_1,T_2)$, versus the reduced velocity c. The cross section $\sigma(g)$ is assumed to be constant ($= 1$). $K_0^* = v_1\sigma(v_1)$ would be the result for a scattering gas at rest.

$v_1 \rightarrow 0$, K^* becomes the usual thermal rate constant for the temperature $T^* = T_2\mu/m_2$. This lower temperature T^* results from the simplifying assumption, that all primary ions move with the same velocity v_1. In contrast to $\bar{\sigma}(v_1)$, $K^*(v_1)$ is always finite; its derivative dK^*/dv_1 vanishes for $v_1 \rightarrow 0$ if $T_2 \neq 0$. As an illustration, fig. 7 shows $K^*(v_1)$ in the case that $\sigma(g)$ is constant

$$K^*(c) = (c + 1/2c)\,\mathrm{erf}(c) + \pi^{-1/2}\exp(-c^2), \qquad (16)$$

with $c = v_1/(2kT_2/m_2)^{\frac{1}{2}}$, and also the limit K_0^* for a scattering gas at rest. For $\sigma \propto g^{-1}$, $K^*(v_1)$ is constant and temperature-independent ($K^* = K_0^*$). The comparison shows, that deviations from a $\sigma \propto g^{-1}$ law tend to be underestimated at low energies.

Fig. 8 is condensed from results of several separate runs under different conditions of the apparatus. For clarity, the host of measured points is omitted; instead, statistical limits (broken lines) are given, which include more than 90% of these points. The absolute error, an estimated ± 20%, is mainly due to the uncertainty of the pressure determination at the low working pressures ($0.3–1.1 \times 10^{-4}$ torr), that were chosen to minimize the rate of secondary processes. The length of the horizontal bar, $2(kT_2/m_2)^{1/2}$, represents the ap-

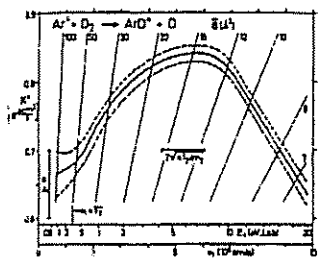

Fig. 8. Cross sections and rate constants K^* for the reaction $Ar^+ + D_2 \rightarrow ArD^+ + D$. The oblique lines connect points of equal cross section $\bar{\sigma}$. Collision energies are not specified because of the broad and asymmetric distributions, that belong to each nominal collision energy $E^* = \frac{1}{2}\mu v_1^2$. A flowing afterglow result [23] is designated FA.

proximate range of velocities g, that contribute to a measurement at any v_1.

Our results show some deviations from the constant reaction rate that is predicted by the Gioumousis and Stevenson model [22]. At low energies they are in good agreement with a flowing afterglow measurement at 300 K [23] but fall short of the values from most mass-spectrometer measurements by typically 25% (for a compilation and critical discussion of earlier results see Henchman [24]). A tentative explanation is, that the relative abundance of excited Ar^+ species in our beam may be similar to that in a following afterglow tube, while it may be different in experiments with conventional electron-impact ion sources. Chupka and Russel [25] have derived from photoionization experiments that the cross section for the reaction $Ar^+ + H_2 \rightarrow ArH^+ + H$ is approximately 30% higher for Ar^+ in the $(^2P_{1/2})$ state than in the $(^2P_{3/2})$ ground state, and a similar ratio might be expected for the reaction with D_2.

At thermal energies, the Langevin close collision rate constant (1.09×10^{-9} cm^3 s^{-1} [22]) is expected to be a reliable upper bound for the total reaction rate constant, that is independently valid for any Ar^+ state. If we now adopt the above ratio of cross sections $\sigma(^2P_{1/2})/\sigma(^2P_{3/2}) \approx 1.3$ for the reaction $Ar^+ + D \rightarrow ArD^+ + D$, then this would put an upper bound of $1.09/1.3 = 0.84 \times 10^{-9}$ cm^3 s^{-1} to the rate constant for ground state ions and of 0.92×10^{-9} cm^3 s^{-1} for a mixture, that is composed of $^2P_{3/2}$ and $^2P_{1/2}$ states according to the statistical weights (2:1). In addition, the competitive exothermic process $Ar^+ + D_2 \rightarrow Ar + D_2^+$ must be taken into account, which, according to preliminary measurements in this laboratory, has a cross section that is approximately 10% of the total reaction cross section. Both these considerations favor a value for $Ar^+ + D_2 \rightarrow ArD^+ + D$, that is lower than the majority of the mass spectrometer results.

From low to medium energies, we observe an increase of the rate constant, again in (qualitative) agreement with the flowing afterglow results mentioned above, where an increase was stated for ruling temperatures, and in contrast to low pressure mass spectrometer studies, where a rate constant was found, that is almost independent of the repeller voltage [26]. One explanation for the observed increase could be, that the cross section for close collisions, defined by the crossing of the centrifugal barrier, is larger than the Langevin cross section in this energy region, while the reaction probability remains virtually constant. If the polarization potential is considered exclusively, then the critical radius, that is the radius of the maximum of the critical centrifugal barrier for the given energy, will decrease from 4 to 2 Å when the energy E_1 is increased from 0.31 to 5 eV. But, most probably, an additional attractive potential has to be taken into account before the smaller distance is reached, that will enlarge the critical radius and in turn the close collision cross section.

The decrease of the rate constant from medium ($E_1 \approx 5$ eV) to higher energies has already been observed and discussed by several other workers [24].

For the endothermic reaction $Ne^+ + CO \rightarrow Ne + C^+ + O$ a well-pronounced threshold can be expected, because of the total dissociation of the products, and not a densely-spaced series of threshold for individual vibrational and rotational states. Measurements [6] and calculations on the basis of the statistical phase-space theory [29] have been published.

In our experiment (fig. 9) the kinetic energy-distribution of the primary beam was smaller than 0.1 eV fwhm; therefore, the energy smearing is almost completely due to the thermal motion of the CO gas in the scattering chamber. There is still some uncertainty about the relative abundance of the doublet states.

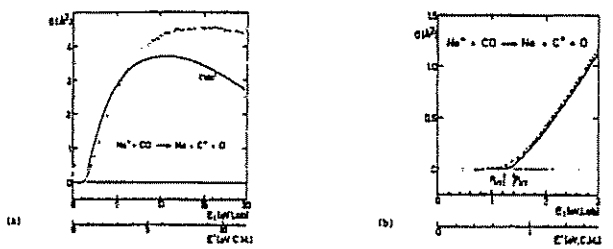

Fig. 9. Cross sections for $Ne^+ + CO \rightarrow Ne + C^+ + O$. The solid line in (a) is a prediction by the phase-space theory, designated calc in the original publication (Light and Lin [29]). It has been extracted from a small graph and may therefore be somewhat in error. (96) is an enlargement of the threshold region. The broken line represents an effective cross section, that has been calculated from the assumed true cross section (solid line) by convolution. E is the nominal collision energy $E_{lab}m_i/m_t$.

$Ne^+(^2P_{3/2})$ and $Ne^+(^2P_{1/2})$, in our primary beam corresponding to endothermicities of 0.817 eV and 0.72 eV respectively [31, 32]. An attempt has been made to construct the true cross section out of the measured effective cross section (fig. 9b, solid line). The analytical form of this curve is

$$\sigma \propto 2(E_1 - 1.40\ \mathrm{eV})^{5/4} + (E_1 - 1.23\ \mathrm{eV})^{5/4}. \qquad (17)$$

where the value zero is assigned to either term if its bracket is negative. The effective cross section, that is computed for this curve (broken line), is a good fit to the experimental points. A deconvolution of experimental data, such as this, is by no means unambiguous, but the figure indicates, that $Ne^+(^2P_{1/2})$ ions are present in our experiment and cause reactions, and that activation energies exceeding endothermicities are not required.

The (5/4)-power fit cannot be regarded as evidence for a (5/4)-power threshold law (which is predicted for certain rearrangement collisions by phase space theory [27–29]). It has been shown that a threshold law would be valid only in a small region near the threshold [30], where the deconvolution of our data is very uncertain.

Acknowledgement

We are indebted to Professor Ch. Schlier for continuous encouragement and many helpful discussions. Also, we thank R. Werner, R. Bahr, H. Hügel, E. Ludwig and W. Ruf, who have at different times participated in the construction and testing of the apparatus, and to Dr. K. Strein, who has confirmed and extended earlier measurements. Substantial funds have been granted by Deutsche Forschungsgemeinschaft (DFG) which have made this work possible.

References

[1] E. Lindholm, in: Ion–molecule reactions in the gas phase, ed. R.F. Gould (Am. Chem. Soc., 1966) p. 1.
[2] E.W. McDaniel, V. Čermák, A. Dalgarno, E.E. Ferguson and L. Friedman, Ion–molecule reactions (Wiley, New York, 1970) pp. 125–138.
[3] M. Henchman, in: Ion–molecule reactions, ed. J.L. Franklin, Vol. 1 (Butterworth, London, 1972) pp. 125–131.
[4] E. Lindholm, in: Ion–molecule reactions, ed. J.L. Franklin, Vol. 2 (Butterworth, London, 1972) pp. 461.
[5] J.P. Futrell and T.O. Tiernan, in: Ion–molecule reactions, ed. J.L. Franklin, Vol. 2 (Butterworth, London, 1972) pp. 485–487.
[6] C.F. Giese and W.B. Maier II, J. Chem. Phys. 39 (1963) 197, 739.
[7] W.B. Maier II, J. Chem. Phys. 42 (1965) 1790; 54 (1971) 2732.

[8] I.I. Leventhal and L. Friedman, J. Chem. Phys. 49 (1968) 1975, 50 (1969) 2928.
[9] M. De Paz, J.J. Leventhal and L. Friedman, J. Chem. Phys. 51 (1969) 3748.
[10] W. Paul, H.P. Reinhard and U. von Zahn, Z. Physik 152 (1958) 143.
[11] E. Fischer, Z. Physik 156 (1959) 16.
[12] K. Rettinghaus, Z. Angew. Phys. 22 (1967) 321.
[13] P.H. Dawson and N.R. Whetten, in: Advances in electronics and electron physics, Vol. 27 (Academic Press, New York, 1969) pp. 59–185.
[14] L.D. Landau and E.M. Lifshitz, Theoretical physics, Vol. 1 (Pergamon, Oxford, 1960) p. 93.
[15] H.G. Dehmelt, in: Advances in atomic and molecular physics, ed. D.R. Bates, Vol. 3 (Academic Press, New York, 1967) pp. 53–72.
[16] W. Schütze and F. Bernhard, Z. Physik 145 (1956) 44.
[17] N.R. Daly, Rev. Sci. Instr. 31 (1960) 264.
[18] K. Barkling, R. Halbing, K. Kramer, H. Pauly, Ch. Schlier and P. Toschek, Z. Physik 166 (1962) 406.
[19] P. v. Busch, H.J. Strunck and Ch. Schlier, Z. Physik 199 (1967) 318.
[20] P.J. Chantry, J. Chem. Phys. 55 (1971) 2746.
[21] P. Langevin, Ann. Chim. Phys. 5 (1905) 245.
[22] G. Glockler and D.P. Stevenson, J. Chem. Phys. 29 (1958) 294.
[23] N.G. Adams, D.K. Bohme, D.B. Dunkin and F.C. Fehsenfeld, J. Chem. Phys. 52 (1970) 1951.
[24] M. Henchman, in: Ion–molecule reactions, ed. J.L. Franklin, Vol. 1 (Butterworth, London, 1972) pp. 179–181, 194, 206–208, 242.
[25] W.A. Chupka and M.E. Russel, J. Chem. Phys. 49 (1968) 5426.
[26] D.O. Stevenson and D.O. Schissler, J. Chem. Phys. 29 (1958) 282.
[27] J.C. Light, J. Chem. Phys. 40 (1964) 3221.
[28] P. Pechukas and J.C. Light, J. Chem. Phys. 42 (1965) 3281.
[29] J.C. Light and J. Lin, J. Chem. Phys. 43 (1965) 3209.
[30] D.G. Truhlar, J. Chem. Phys. 51 (1969) 4617.
[31] J.L. Franklin, J.G. Dillard, H.M. Rosenstock, J.T. Herron and K. Draxl, NSRDS - NBS 26 (U.S. Dept. of Commerce, 1969).
[32] R. de B. Darwent, NSRDS - NBS 31 (U.S. Dept. of Commerce, 1970).
[33] U. Nowotny, E. Teloy and Ch. Schlier, to be published.

ACKNOWLEDGEMENTS

We are indebted to Professor A.K. Barua for his kind interest. The experimental assistance of Mr. D. Shome is gratefully acknowledged.

REFERENCES

1 S.W. Nagy, W.J. Savola and E. Pollack, Phys. Rev., 177 (1969) 71.
2 B.L. Moiseiwitsch, Proc Phys. Soc. London, Ser A, 69 (1956) 653
3 A.E. DeVries and P.K. Rol, Vacuum, 15 (1965) 135.
4 J.B. Hasted and J.B.H. Sladeford, Proc. R. Soc. London, Ser. A, 277 (1955) 466

International Journal of Mass Spectrometry and Ion Physics, 42 (1982) 195–211 195
Elsevier Scientific Publishing Company, Amsterdam — Printed in The Netherlands

THE EFFECTIVE CONTAINMENT OF PARENT IONS AND DAUGHTER IONS IN TRIPLE QUADRUPOLES USED FOR COLLISIONAL DISSOCIATION

P.H. DAWSON

Physics Division, National Research Council, Ottawa, Ont. K1A 0R6 (Canada)

J.E. FULFORD

Sciex Inc., 55 Glen Cameron Rd., Thornhill, Ont. L3T 1P2 (Canada)

(First received 25 September 1981; in final form 12 November 1981)

ABSTRACT

Since triple quadrupoles are becoming widely used in analytical applications of low energy collisionally-induced dissociation mass spectrometry (MS/MS), a clear understanding of the role of the radiofrequency (*r.f.*) only quadrupole is of paramount importance. This paper presents experimental results, supported by theoretical calculations, which demonstrate how a well-designed system can be operated with very low ion losses so that quantitative measurements can be made. Ion containment was studied as a function of applied *r.f.* voltage and the effects of gas scattering and of the sudden change in ionic mass during ion fragmentation were evaluated. The results allow some insight into the problem of establishing standard operating conditions for collecting library spectra and emphasize the importance of some of the design-dependent variables.

INTRODUCTION

Triple quadrupoles [1—5] are becoming widely used in analytical applications of collisionally-induced dissociation (CID) mass spectrometry (MS/MS) where rapid unambiguous identification is required. Ions of a single mass to charge ratio are selected from the mass spectrum by the first quadrupole; these ions are contained within a second quadrupole field where they undergo fragmentation by collision with a target gas and the daughter ions are analysed in the third quadrupole. It is important in the rapid development of the technique of *MS/MS* using triple quadrupoles, that the containment of parent ions and daughter ions by the central quadrupole be well understood [6,7]. This is particularly true if CID spectral libraries are to be accumulated under standardized conditions [8]. As will be demonstrated later, the choice of operating conditions can dramatically influence the observed spectra and, yet, if conditions are well chosen, high efficiency ion containment and high transmission of daughters can be achieved. Design of

0020-7381/82/0000—0000/$02.75

the central quadrupole and the chosen modes of scanning spectra become important [6].

The triple quadrupole system is also being used for quantitative measurements of ion dissociation by collision [9] and of ion–molecule declustering [10]. It is vital in such measurements to understand any limitations that may be imposed by ion scattering or by the transformation of the parent ion to an ion of different (usually lower) mass.

This paper presents a general discussion of theoretical and experimental results which characterize ion containment in quadrupoles operated in the radiofrequency (r.f.) only mode. The experimental measurements are in good agreement with the theoretical calculations of:

(1) the containment as a function of r.f. voltage (q_z);

(2) the effects of gas scattering;

(3) the effects of the sudden change of ionic mass as the parent is fragmented.

It is shown that a well-designed and operated system can have very low losses so that quantitative measurements can be made. The effect of the transverse oscillations in extending the ion path length is also considered since this can introduce corrections to the measured cross-sections for collisionally induced dissociation.

THEORETICAL BACKGROUND

Only the containment of ions by the central quadrupole (QUAD 2) will be considered here. Figure 1(a) shows a sketch of the apparatus [11] used in this type of measurement and Fig. 1(b) shows the automatic control system and provides a set of symbols which will be used in this discussion. The interfacing of QUAD 2 with QUAD 1 and QUAD 3 presents a very complex series of ion-optical problems the theoretical approach to which has been very briefly discussed elsewhere [12]. It has also been shown experimentally [7–10] that with properly designed coupling of the quadrupoles, high transmission between the quadrupoles can be achieved, so that QUAD 1 will be considered here only as a source of ions for QUAD 2. In some instruments, one or more apertures are used to isolate the central quadrupole and limit gas flow into the analysing quadrupoles. The influence of apertures between QUAD 2 and QUAD 3 will be discussed.

Quadrupole operation [13] is always best examined in terms of the universal Mathieu parameters a and q which automatically take into account the mass to charge ratio (m/z) of the ion under consideration, the applied angular frequency (ω), the applied d.c. (U) and r.f. ($V \cos \omega t$) voltages and the size of the quadrupole field (half the rod-separation = r_0) since

$$a = 4zU/mr_0^2\omega^2 \quad (1)$$

$$q = 2zV/mr_0^2\omega^2 \quad (2)$$

Fig. 1. (a) Schematic of the TAGA 6000 MS/MS system. (b) TAGA 6000 interface and control system

The discussion is further generalized by considering the transverse displacement of the ions in either coordinate direction u, in units of r_0 and transverse velocities in terms of $u' = du/d\xi$, where $\xi = \omega t$. The length of the quadrupole field is defined in terms of the number of r.f. cycles (n) that an ion takes to pass through the quadrupole. In a perfect quadrupole field, the longitudinal velocity is unaffected by the field. The properties of the quadrupole field are summarized [13] in a stability diagram (Fig. 2) which identifies those regions of (a, q) space where the ions have mathematically stable trajectories. Inside the stable region, the iso-β lines for the two transverse directions (x and y) indicate operating points where the ion trajectories contain the

Fig. 2. Stability diagram in (a, q) space for transverse oscillations in the quadrupole field

same frequency components. The limits to stability are $\beta = 0$ and $\beta = 1$. The principal frequencies of the ion oscillation are $\beta\omega/2$ and $(1 - \beta)\omega/2$. For example, when β is small, the number of r.f. cycles in the characteristic half-beat length is $1/\beta$. QUAD 2 is normally operated with only an r.f. voltage applied ($a = 0$) to ensure the containment of ions of a wide range of m/z values. In theory, all ions with $q < 0.91$ then have stable trajectories. In practice, ions will be lost only when $q > 0.91$ if there is sufficient time (i.e. a large enough) for the transverse displacement to grow exponentially to a value greater than r_0. Even if $q < 0.91$, an ion may not be contained if its initial displacement u_0 and its initial transverse velocity $\dot{u}_0$ are such that somewhere along the trajectory the displacement u exceeds unity (i.e. actual displacement $> r_0$). The combinations of values of u_0 and $\dot{u}_0$ that lead to ion transmission are sometimes referred to as the acceptance [14] of the quadrupole in the phase plane (Fig. 3). These are described in more detail below. The concept of ion acceptance is invaluable in these discussions since it allows the examination of ion transmission as a whole and it is not necessary to examine the details of individual ion trajectories. The nature of the ion acceptance depends upon the phase of the r.f. field at the moment under consideration.

One immediate limitation to the storage of daughter ions is evident from the stability diagram of Fig. 2. If QUAD 2 has an r.f. voltage applied such that the parent ion of mass M_p has a value q_p, then daughter ions will, in principle, only be observed if their q value (q_d) is <0.908, i.e. if their mass $M_d > M_p q_p/0.908$. Some early instruments have been operated with a fixed r.f. voltage applied to QUAD 2. In those cases, the low mass end of the daughter spectrum was unlikely to be observed. A fixed r.f. voltage would also give a variation in q_p as the parent mass spectrum is scanned and this can lead to variable storage efficiency (see below). In automated instruments two modes of mass scanning with variable r.f. voltage have been used [6–8].

In the first the r.f. applied to QUAD 2 ($(r.f.)_2$) is set in a fixed ratio to that being applied during the scanning of QUAD 1. (QUAD 1 operates with $q_p = 0.706$). This is the 'constant q parent scan'. In the second, $(r.f.)_2$ is set in a fixed ratio to that being applied for the daughter ion in QUAD 3. This is the 'constant q daughter scan' (see Fig. 1(b)).

The acceptance of ions by QUAD 2 has been calculated for a number of values of q when $a = 0$. Methods of calculation are described elsewhere [12–14]. The combinations of initial position and initial transverse velocity that lead to ion transmission (in a 'long' field) are contained within acceptance ellipses. Figure 3 shows some examples for $q = 0.2$, $q = 0.6$ and $q = 0.85$. Ten different initial phases of the r.f. field are illustrated. The ellipse equations are usually represented as

$$Fu^2 + 2Guu + Bu^2 = \varepsilon$$

where the acceptance (or emittance) ε is equal to the ellipse area divided by π. The area does not depend on the phase of the field. The emittance is a measure of the ability of the quadrupole to transmit ions. In an idealized case, the acceptance area would be uniformly populated with ions.

The ellipses of Fig. 3 equally represent the possible distributions of transverse positions and velocities at a given field phase at any point along QUAD 2.

The filling of the acceptance ellipses will depend upon how the emittance of QUAD 1 matches the acceptance of QUAD 2 and the phase relation between these two, the extent of coupling in the fringing fields between quadrupoles and so on. In general terms, the situation is somewhat similar to the coupling of an ion source to a conventional single quadrupole [12–14]. If the acceptance of QUAD 2 is large compared with the emittance of QUAD 1, its variation with q will not be important (source limited conditions). If the acceptance of QUAD 2 is smaller than the effective emittance of QUAD 1, it will become limiting (equivalent to analyser limited conditions).

The acceptance ellipses will be used as the basis for the theoretical modelling of the three questions which arise in ion containment. These are (a) how does storage of parent ions depend upon q_p, (b) how does a change in transverse velocity, which might be brought about by gas scattering, affect ion containment and how does it depend upon q_p and (c) how does the sudden change from q_p to q_d affect ion storage and what is its dependence upon the q values.

THE EXPERIMENTAL SYSTEM

The measurements were made with a prototype TAGA 6000 triple quadrupole [11]. This has been described elsewhere [15] and its operating characteristics have been outlined [6–7]. The collision conditions in this instru-